ARTICLE

Molecular Nanocomposites with Lanthanide- and Counter-Cation-Mediated Interfacial Electron Transfer between Phthalocyanine and Polyoxovanadate

Irina Werner,[a] Jan Griebel,[a] Albert Masip-Sánchez,[b] Xavier López,*[b] Karol Załęski,[c] Piotr Kozłowski, *[d] Axel Kahnt,[a] Martin Boerner,[a,e] Ziyan Warneke,[a,f] Jonas Warneke,[a,f] and Kirill Yu. Monakhov*[a]

A series of {V₁₂}-nuclearity polyoxovanadate cages covalently functionalised with one or sandwiched by two phthalocyaninato (Pc) lanthanide (Ln) moieties *via* V–O–Ln bonds were prepared and fully characterised for paramagnetic Ln = Sm^{III}–Er^{III} and diamagnetic Ln = Lu^{III}, including Y^{III}. The LnPc-functionalised {$V_{12}O_{32}$} cages with fully-oxidised vanadium centres in the ground state were isolated as (nBu₄N)₃[HV₁₂O₃₂Cl(LnPc)] and (nBu₄N)₂[HV₁₂O₃₂Cl(LnPc)₂] compounds. As corroborated by a combined experimental (EPR, DC and AC SQUID, laser photolysis transient absorption spectroscopy, electrochemistry) and computational methods (DFT, MD, model Hamiltonian approach), the compounds feature *intra*- and *inter*molecular electron transfer that is responsible for a partial reduction at V(3d) centres from V^V to V^{IV} in the solid state and at high sample concentrations. The effects are generally Ln-dependent and are clearly demonstrated for the (nBu₄N)₃[HV₁₂O₃₂Cl(LnPc)] representative with Ln= Lu^{III} or Dy^{III}. *Intra*molecular charge transfer takes place for Ln = Lu^{III} and occurs from a Pc ligand *via* the Ln centre to the {$V_{12}O_{32}$} core of the same molecule, whereas for Ln= Dy^{III} only *inter*molecular charge transfer is allowed, which is realised from Pc in one molecule to {$V_{12}O_{32}$} core of another molecule usually *via* the nBu₄N⁺ counter-cation. For all Ln but Dy^{III} two of these phenomena may be present in different proportions. Besides, it is demonstrated that (nBu₄N)₃[HV₁₂O₃₂Cl(DyPc)] is a field induced single molecule magnet with a maximal relaxation time of order 10^{-3} s. The obtained results open up the way to further exploration and fine-tuning of these three-modular molecular nanocomposites regarding tailoring and control of their Ln-dependent charge-separated states (induced by *intra*molecular transfer) and relaxation dynamics as well as of electron hopping between molecules. This should enable to realise ultra-sensitive polyoxometalate powered quasi-superconductors, sensors and data storage/processing materials for quantum technologies.

Introduction

Polyoxometalates (POMs),[1] molecular metal–oxides, show well-defined nanoscale spatial structures[2] carrying a negative charge that is balanced by surrounding counterions.[3] In solution, these inorganic complexes tend to spontaneously form low-to-high dimensional self-assemblies, exploiting forces between different weakly interacting particles (POM, cation, solvent molecule).[4] Introducing an organic

a. *Leibniz Institute of Surface Engineering (IOM), Permoserstr. 15, 04318 Leipzig, Germany. E-mail: kirill.monakhov@iom-leipzig.de*

b. *Universitat Rovira i Virgili, Departament de Química Física i Inorgànica, Marcel·lí Domingo 1, 43007 Tarragona, Spain. E-mail: javier.lopez@urv.cat*

c. *NanoBioMedical Centre, Adam Mickiewicz University in Poznań ul. Wszechnicy Piastowskiej 3, 61-614 Poznań, Poland*

d. *Institute of Spintronics and Quantum Information, Faculty of Physics, Adam Mickiewicz University in Poznań, ul. Uniwersytetu Poznańskiego 2, 61-614 Poznań, Poland. E-mail: kozl@amu.edu.pl*

e. *Institute of Inorganic Chemistry, Leipzig University, Johannisallee 29, 04103 Leipzig, Germany.*

f. *Wilhelm-Ostwald-Institute for Physical and Theoretical Chemistry, Leipzig University, Linnéstr. 2, 04103 Leipzig, Germany.*

functionality onto POM[5–7] provides an additional and most effective lever for controlling and programming these interactions at the charge- and spin-state[8,9] level. Such an interplay between POM's coordination and supramolecular[10] chemistry and POM's electronic structure[11] opens up a wide range of possibilities for developing early models of functional hybrid quantum systems, with POMs as spin qubits or POMs as quantum sensors. The POM-based devices would thus enable to store, process, or sense the information through cooperative *intra*- and *inter*molecular effects.

The covalent combination of POMs with transition metal (TM) or lanthanide[12,13] (Ln) ions embedded into redox-active phthalocyanine (Pc²⁻) macrocycles has emerged as a good compromise to address this challenge. Unlike the well-described electrostatic interactions of phthalocyanines and POMs,[14–19] there are only a few reports addressing effects of their covalent interaction.[20,21] Drain and co-workers synthesised hybrid compounds[20] (nBu₄N)₅[PW₁₁O₃₉(TMPc)] (TM = Zr⁴⁺ or Hf⁴⁺) where a transition metal–Pc moiety is directly grafted onto the fully-oxidised, lacunary Keggin-type POM. It was demonstrated that the metal ions mediate the electronic communication between the Pc and the Keggin-POM units. Later, the LnPc-function-

ARTICLE

alised analogues, $[PW_{11}O_{39}(LnPc)]^{6-}$ (Ln = Tb[III], Dy[III] and Y[III]) were introduced by Kögerler and co-workers, whereby for the Dy[III]-containing species slow relaxation of the magnetisation was observed.[21] In two other related studies, we delivered appealing pre-conditions for building up stimuli-responsive POM quantum networks based on LnPc-functionalised POMs with fully-oxidised V(3d) centres[22] and/or reduced vanadyl (VO^{2+}) groups[23,24] (hereafter referred to as V-POMs[25]). Firstly, we showed[26] that compounds consisting of the electron-donor phthalocyaninato lanthanide moiety and the electron-acceptor V_3-substituted Wells-Dawson-type POM structure, linked covalently to each other *via* a pyridine-augmented tris(alkoxo) ligand, exhibit *intra-* and *inter*molecular ground-state charge transfer. It might thus be used to tailor electron communication within quantum networks. Secondly, enabling direct interaction between V-POM and LnPc we succeeded[27] in the synthesis of structurally robust, electron correlated compounds $[V_{12}O_{32}Cl(YbPc)_n]^{n-5}$ (n = 1 or 2), in which the dodecavanadate cage is covalently capped by one or sandwiched by two YbPc moieties. Building upon this work,[27] we now report on a broad spectrum of unique chemical physics of $[HV_{12}O_{32}Cl(LnPc)_n]^{n-4}$ compounds for Ln = Sm[III]–Er[III], Lu[III] and Y[III] (hereafter referred to as PcLn-{V_{12}} for n = 1 and (PcLn)$_2$-{V_{12}} for n = 2) using a combination of experimental and computational techniques.

It is noteworthy that the fully-oxidised, lacunary-type {$V_{12}O_{32}$}-cage[28] has been shown in numerous studies to be an excellent scaffold for functionalisation with 3d-,[29–31] 4f-[32–34] and alkaline-earth metal ions.[35–37] Cronin and co-workers were first to present a series of $(nBu_4N)_2[LnV_{12}O_{32}Cl](H_2O)_2(CH_3CN)_2$ compounds with late Ln ions (Gd[III]–Er[III]) directly incorporated into the dodecavanadate cage.[33] Magnetic measurements revealed, however, the free Ln ion behaviour. Practically simultaneously, Powell and co-workers described an unusual cationic version of the {V_{12}}-nuclearity cage functionalised with two Ln ions (Ln = Gd[III]–Er[III]).[34] An elegant method for the synthesis of metal functionalised $[V^V_{12}O_{32}Cl]^{5-}$ using a "placeholder" strategy was introduced by Streb and co-workers.[29–32,36,37] For instance, stepwise functionalisation of $(nBu_4N)_3(Me_2NH_2)_2[V_{12}O_{32}Cl]$, where the dimethylammonium cation assumes the placeholder function, with transition metal ions[29–31] or with an early Ln[32] representative Ce[III] resulted in mono- and bis-substituted vanadium–oxo clusters with enhanced redox activity. This ability of the $[V^V_{12}O_{32}Cl]^{5-}$ polyoxoanion to act as an electron reservoir, without undergoing substantial structural transformation,[38] was also used to stabilise low-valent Fe[I] species.[31]

In this Article, we showcase the underlying formation and mechanism of action of highly promising donor–acceptor nanocomposites consisting of one or two LnPc moieties ligated to the {$V_{12}O_{32}$} cage (Fig. 1). The produced mono-substituted $(nBu_4N)_3[HV_{12}O_{32}(Cl)](LnPc)$ (hereafter referred to as PcLn-{V_{12}}) and bis-substituted $(nBu_4N)_2[HV_{12}O_{32}(Cl)](LnPc)_2$ (hereafter referred to as (PcLn)$_2$-{V_{12}}) compounds feature the *intra*molecular charge transfer and redox-promoted magnetism. The electron communication between the individual compounds containing paramagnetic Sm[III]–Er[III] or diamagnetic Lu[III] and Y[III] ions is realised within their supramolecular self-assembly that is generated due to *inter*molecular interactions involving

V-POM, LnPc, and counterion units. The future controlled immobilisation, electronical modification, and electrical contacting of these nanocomposites on surfaces might lead to the creation of scalable 'molecularly powered quantum network-on-a-chip' electronics for neurocomputing and ultra-sensitive electrical and magnetic signal detection.
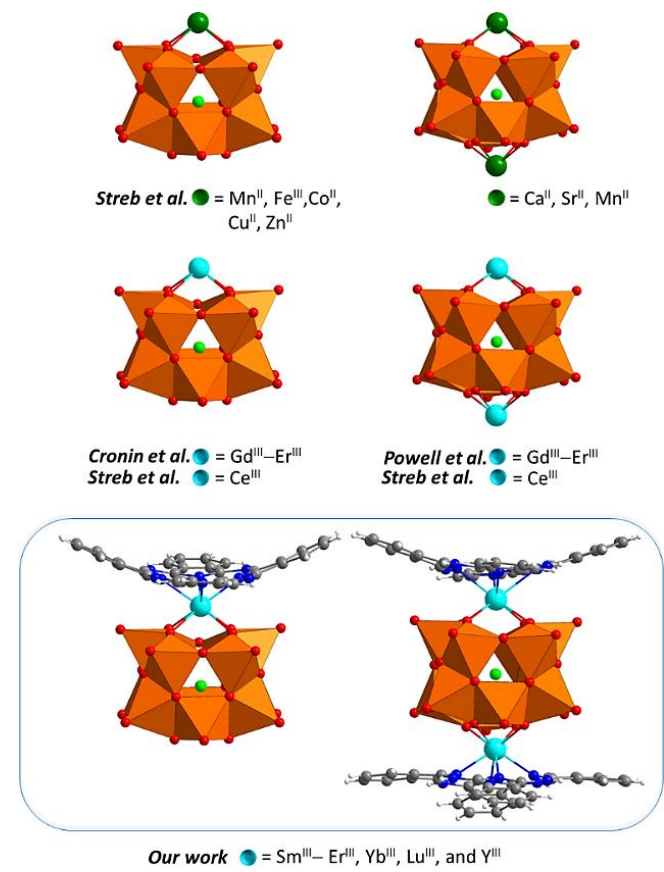

Fig. 1. An overview of literature-known mono- and bis-heterometal-functionalised {$V_{12}O_{32}$} cages (top and middle) and new (PcLn)$_n$-{V_{12}} hybrids with n = 1 or 2 (bottom). Colour code: VO_5 polyhedra = orange, O = red, Cl = green, C = dark grey, N = blue, H = white. Solvent ligands (top and middle), counterions (in all examples), and H atoms at the {$V_{12}O_{32}$} cage (bottom) are not shown.

Results and Discussion

Synthesis and structure characterisation

Monophthalocyanine lanthanide acetate complexes (PcLnOAc) with Ln = Sm[III]–Er[III], Lu[III] and Y[III] were synthesised similarly to the protocols described in the literature.[39,27] Repeated purification by column chromatography and subsequent slow evaporation of PcLnOAc·MeOH·H$_2$O in wet ethanol delivered high-quality PcLnOAc·EtOH·H$_2$O crystals for Ln = Sm[III], Dy[III], Lu[III] and Y[III] (see the ESI[+]). The synthesis of PcLnOAc with earlier lanthanides (Ln = La[III]–Nd[III]) was not successful likely due to their larger ionic radii.

The subsequent reaction of one or two equivalents of PcLnOAc·MeOH·H$_2$O with $(nBu_4N)_4[HV_{12}O_{32}Cl]$[28] was carried out

according to the synthetic routes developed in our previous Communication[27] for $[V_{12}O_{32}Cl(YbPc)_n]^{n-5}$ with $n = 1$ or 2 (see the ESI†). CHN elemental analysis, thermogravimetric (TG) measurements, IR- and UV-Vis-spectroscopy and ^1H NMR spectra (for PcLu-{V_{12}}) of powder samples confirmed the identity and the purity of the synthesised compounds as well as the presence of three and two nBu$_4$N$^+$ counter-cations *per* {V_{12}} in PcLn-{V_{12}} and (PcLn)$_2$-{V_{12}} compounds, respectively (see the ESI†).

Needle-shaped green crystals, suitable for X-ray analysis were obtained for (nBu$_4$N)$_3$[HV$_{12}$O$_{32}$Cl(YPc)](CH$_3$CN)$_4$ by slow diffusion of di-*iso*-propylether into an acetonitrile solution. In the case of bis-substituted compounds plate-shaped blue crystals with the formula (nBu$_4$N)$_3$[V$_{12}$O$_{32}$Cl(LnPc)$_2$](CH$_3$CN)$_3$ (Ln = Dy^{III}, Ho^{III}) were isolated by slow evaporation of an acetonitrile / dichloromethane solution (see the ESI†).

High resolution negative-mode ESI-MS of PcLn-{V_{12}} and (PcLn)$_2$-{V_{12}} also confirmed in both cases the presence of the corresponding compounds (see the ESI†). For example, in the ESI mass spectrum of PcLu-{V_{12}} alongside with the [HV$^V_{12}$O$_{32}$(Cl)](LuPc)]$^{3-}$ ion, containing a fully-oxidised {V_{12}O$_{32}$} cage, a mixture of [(nBu$_4$N)$_2$[HV^{IV}V$^V_{11}$O$_{32}$Cl](LuPc)]$^{2-}$ / [(nBu$_4$N)$_2$[V$^V_{12}$O$_{32}$Cl](LuPc)]$^{2-}$ in a ratio of 1:1 combining both the fully-oxidised and the one-electron-reduced vanadium–oxo clusters, respectively, was detected. Signals indicating the presence of the one-electron-reduced {$V^{IV}V^V_{11}$}, core in PcLn-{V_{12}} could also be observed in Eu^{III}-, Gd^{III}-, Tb^{III}- and Dy^{III}-analogues. In nearly all bis-substituted (PcLn)$_2$-{V_{12}} derivatives the prevailing number of signals was attributed to the ions with a {$V^{IV}V^V_{11}$} electron population.

For both PcLu-{V_{12}} and (PcLu)$_2$-{V_{12}} molecular nanocomposites, X-ray photoelectron spectroscopy (XPS) of their powder samples confirms the presence of V^{IV}O^{2+} units in the {V_{12}} core. It is evidenced by the presence of a broad structured line with a shoulder in the V2p$_{3/2}$ region (Figs. S53 and S54). O1s/V2p$_{3/2}$ binding energy differences of 12.9 eV and 14.2 eV were assigned to V^V and V^{IV}, respectively. These findings agree with the values reported previously for Ca$_2$-{V_{12}} containing a partially reduced dodecavanadate cage.[36]

Electrochemical analysis

The redox properties of the selected PcLn-{V_{12}} compounds were studied by recording the cyclic voltammograms in CH$_2$Cl$_2$ solution using tetra-n-butylammonium hexafluorophosphate (NBu$_4$PF$_6$) as an electrolyte at a scan rate of 100 mV·s^{-1}. The redox potentials are reported against Fc$^+$/Fc. The comparison of the cyclic voltammograms of PcLu-{V_{12}}, PcGd-{V_{12}} and PcDy-{V_{12}} in the -1 V to $+1$ V potential range shows that the electrochemical properties of the compounds are very similar and feature four quasi-reversible redox processes, namely one reductive transition (R$_1$) and three oxidative processes (O$_1$, O$_2$ and O$_3$). The nature of the lanthanide ion, though, influences slightly the redox activity of the compounds resulting in overall cathodic shifts in Gd^{III}- and Dy^{III}-containing representatives (Fig. 2). Mean

peak potentials for the investigated nanocomposites are listed in Table 1. The nature of compounds' redox waves was determined by comparison with the corresponding precursors, i.e. (nBu$_4$N)$_4$[HV$_{12}$O$_{32}$Cl] and PcLnOAc (Fig. S55). The most interesting feature in all cyclic voltammograms is the appearance of the new redox process O$_1$, which can be assigned to the oxidation of V^{IV} in the {V_{12}O$_{32}$} cage matching earlier reports for one electron-reduced dodecavanadate bis-functionalised with Ce^{III}.[37] (PcLn)$_2$-{V_{12}} compounds show comparable results with those obtained for PcLn-{V_{12}}. For example, the (PcLu)$_2$-{V_{12}} is characterised by small cathodic shifts and low peak-current for all redox processes compared to the mono-substituted derivative (Fig. S55).

Table 1. Overview of the electrochemically studied compounds and their half-wave potentials for each determined redox process.

	R$_1$ / [V] (V^V→V^{IV})	O$_1$ / [V] (V^{IV}→V^V)	O$_2$ / [V] (Pc→Pc$^{•+}$)	O$_3$ / [V] (Pc$^{•+}$→Pc^{2+})
{V_{12}}	-0.37			
PcLu-{V_{12}}	-0.50	-0.07	0.30	0.72
PcGd-{V_{12}}	-0.45	0.00	0.36	0.73
PcDy-{V_{12}}	-0.37	0.00	0.32	0.73

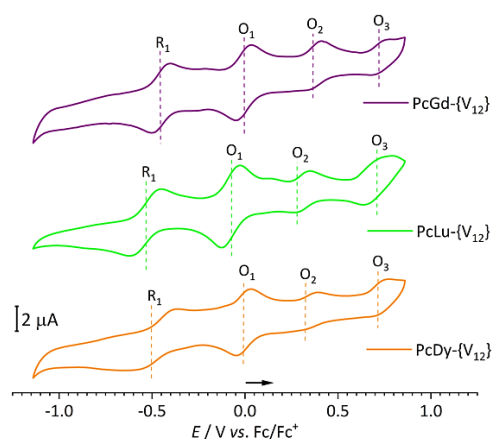**Fig. 2.** Cyclic voltammograms of PcLu-{V_{12}} ($c = 0.4 \times 10^{-3}$), PcGd-{V_{12}} ($c = 0.4 \times 10^{-3}$) and PcDy-{V_{12}} ($c = 0.4 \times 10^{-3}$) in CH$_2$Cl$_2$ solution of NBu$_4$PF$_6$ ($c = 1 \times 10^{-1}$) at the scan rate of 100 mV·s^{-1} *vs.* Fc$^+$/Fc.

Solid-state and solution EPR studies

EPR is a highly sensitive and a powerful tool for detecting unpaired spins in paramagnetic substances and, thus, of utmost importance for monitoring redox events in compounds such as polyoxovanadates,[24] where vanadium ions may simultaneously act as charge and spin carriers. For instance, the striking role of EPR has been demonstrated for non-photoinduced charge transfer between MPc (M = Yb^{III} or Y^{III}) moieties and a {V_3}-substituted Wells-Dawson-type POM, which are linked to each other by an insulating organic spacer.[26] Polycrystalline PcLuOAc showed similar EPR characteristics (Fig. S57), as reported earlier for PcYOAc,[26] featured by an isotropic signal with a *g* value of

2.002 and a line width ΔB_{PP} = 0.38 mT. The shape of the EPR signal and the *g* value point out a ligand-centred (specifically, carbon-centred) freely delocalised electron, excluding other paramagnetic impurities.

Monophthalocyaninato acetate complexes of other paramagnetic lanthanides explored in this study are EPR silent due to very fast spin-lattice relaxation time at room temperature, typical for lanthanide ions. This is in accordance with earlier EPR studies of neutral bis-phthalocyanine lanthanide complexes with a permanent radical character.[40] In the case of PcGdOAc, which is distinguished by its relatively long spin-lattice relaxation time, a broad EPR signal induced by a large spin-spin interaction between Gd^{III} ions was observed (Fig. S57). Concentration-dependent measurements of PcLuOAc in CH_2Cl_2 (Fig. S58) showed that the radical character is barely detectible at very low concentrations. These findings are in accordance with those reported for metal-free phthalocyanines,[41] closed-shell molecules exhibiting condensed-phase paramagnetism, which is typical for planar π-extended systems with high-lying HOMOs.[42]

The solid-state EPR spectra of the equal amounts of polycrystalline powdered samples of PcLu-{V_{12}} and (PcLu)$_2$-{V_{12}} (Fig. 3) display in both cases, beside a radical character (with a *g* value = 2.002 each), a central line with large shoulders with the *g* values of 1.997 and 1.985, respectively. The shape of the signals as well as the calculated *g* values are typical for V^{IV} ions constitutive of polyoxovanadates in which electrons are delocalised over more than one V^{IV} centre.[43–46]
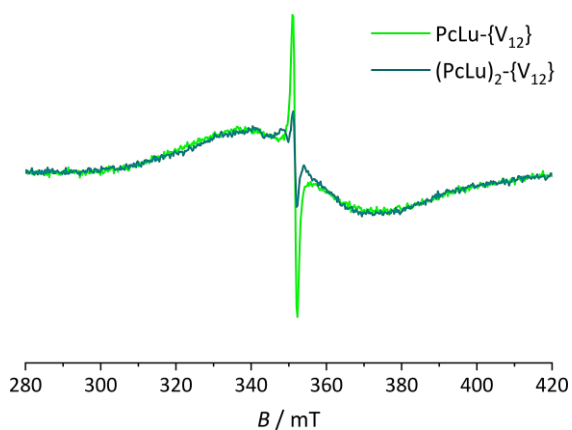

Fig. 3. Solid-state X-band EPR spectra of PcLu-{V_{12}} (green) and (PcLu)$_2$-{V_{12}} (dark cyan) measured at r.t. at a frequency of 9.44 GHz, modulation amplitude of 0.1 mT, and microwave power of 0.2 mW. Normalised double integration values: PcLu-{V_{12}} = 2.97·10^8 (10 mg, 3.7 mmol), (PcLu)$_2$-{V_{12}} = 3.07·10^8 (11.5 mg, 3.7 mmol)

Although the presence of a radical is more pronounced in PcLu-{V_{12}} as compared to (PcLu)$_2$-{V_{12}}, the intensities of the V^{IV} signals are practically similar in both cases.

The analysis of the unit cell packings of PcY-{V_{12}} and (PcDy)$_2$-{V_{12}} (Figs. S62 and S63) showed that both systems feature a layer structure, where the corresponding hybrid anions are separated by the nBu$_4$N$^+$ counter-cations, thus lacking any direct π-π-stacking interactions or hydrogen bonding between the units

as in the case of PcLnOAc. These findings lead to the conclusion that the *inter*molecular charge transfer in the solid state is likely transmitted by nBu$_4$N$^+$ in the systems PcLn-{V_{12}} or (PcLn)$_2$-{V_{12}}. Lately, it has been recognised that the interactions between POMs and counter-cations are not limited to mere charge balance but are also crucial for the structure-induced-reactivity of POMs, charge transport characteristics in molecular junctions and electrical conductivity.[3,47,48]

Solid-state EPR spectra of the equal amounts (each 3.7 mmol) of other polycrystalline powdered samples of paramagnetic PcLn-{V_{12}} and (PcLn)$_2$-{V_{12}} hybrid compounds (Ln = Sm^{III}–Eu^{III}, Tb^{III}–Yb^{III}) revealed only broad V^{IV}-based signals (see Fig. 4 for PcLn-{V_{12}} compounds with the corresponding listed *g* values and normalised double integration values). The EPR spectra of PcGd-{V_{12}} and (PcGd)$_2$-{V_{12}} showed a broad overlap of signals probably originating from V^{IV} and f electrons of Gd^{III}, so that the *g* values could not be determined (Fig. S59).
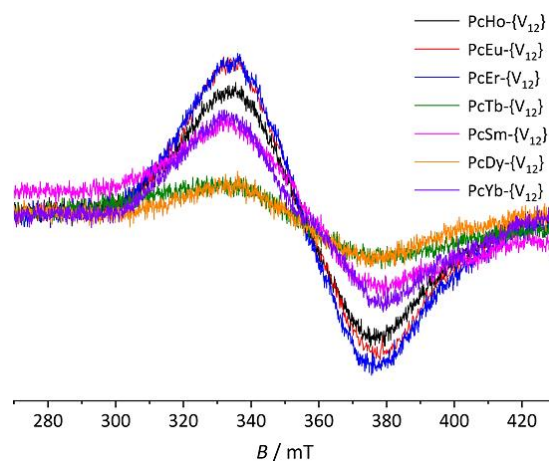

Fig. 4. Solid-state X-band EPR spectra of paramagnetic PcLn-{V_{12}} (Ln = Sm^{III}–Eu^{III}, Tb^{III}–Yb^{III}) with detected V^{IV} signals. Spectra were measured at r.t. at a frequency of 9.44 GHz, modulation amplitude of 0.1 mT, and microwave power of 0.2 mW with the following *g* values: 1.977 (Sm^{III}), 1.984 (Eu^{III}), 1.993 (Tb^{III}), 1.985 (Dy^{III}), 1.984 (Er^{III}), 1.987 (Ho^{III}) and 1.986 (Yb^{III}). Color code: Sm^{III} = magenta, Eu^{III} = red, Tb^{III} = dark green, Dy^{III} = orange, Er^{III} = blue, Ho^{III} = black, Yb^{III} = violet. Normalised double integration values: PcHo-{V_{12}} = 3.12·10^5, PcEu-{V_{12}} = 3.57·10^5, PcEr-{V_{12}} = 3.81·10^5, PcTb-{V_{12}} = 2.56·10^4, PcSm-{V_{12}} = 9.05·10^4, PcDy-{V_{12}} = 1.94·10^4, PcYb-{V_{12}} = 2.48·10^5.

The comparison of the V^{IV} signal integration of the paramagnetic PcLn-{V_{12}} representatives among each other qualitatively shows that in the case of the prolate ions[49] Sm^{III}, Er^{III} and Yb^{III} the spin density is higher than that where highly oblate Dy^{III} and Tb^{III} (except for Ho^{III}) are involved. Further investigations applying high-field EPR at low temperature are the focus of our future research on the quantification of the coupling between the magnetic moments of Ln^{III} ions and the free delocalised electron[50] as well as its impact on the *intra*molecular charge transfer from the LnPc moiety to the {V_{12}} unit.

As a proof-of-concept, that the reduction of the {V_{12}}-nuclearity cage is due to the charge transfer from the Pc moiety, we also

investigated $(nBu_4N)_2[LnV_{12}O_{32}(Cl)](H_2O)_2(CH_3CN)_2$ (Ln = Gd[III], Dy[III], Ho[III], Yb[III] and Y[III]) that were synthesised according to the published procedure[33] (see the ESI[†]) . The compounds proved to be EPR silent, except for Gd[III]-caped $\{V_{12}O_{32}\}$ cage characterised only by the signal with the *g* value of 1.987 (Fig. S60) that is typical for Gd[III] hydrated salts.[51]

Concentration dependent EPR measurements of PcLu-$\{V_{12}\}$ and (PcLu)$_2$-$\{V_{12}\}$ between 1 mM and 20 mM in CH_2Cl_2 showed that in PcLu-$\{V_{12}\}$ a weak radical character is already present at 1 mM, whereas (PcLu)$_2$-$\{V_{12}\}$ is EPR silent at the same concentration. Further increase in concentration was accompanied by a continuous increase of the radical character (up to 10 mM) in both compounds, but only in (PcLu)$_2$-$\{V_{12}\}$ the growth of the V[IV] signals was observed throughout the concentration series (Fig. 5). These findings differ from those observed for these compounds in the solid state, where the intensities of V[IV] signals for both mono- and bis-functionalised derivatives are practically the same. To reveal obviously different underlying mechanisms of *inter*molecular charge transfer in the solid state and in solution, on the one hand, and between PcLn-$\{V_{12}\}$ and (PcLn)$_2$-$\{V_{12}\}$ in solution, on the other hand, we next conducted computational study on these molecular nanocomposites (*vide infra*).
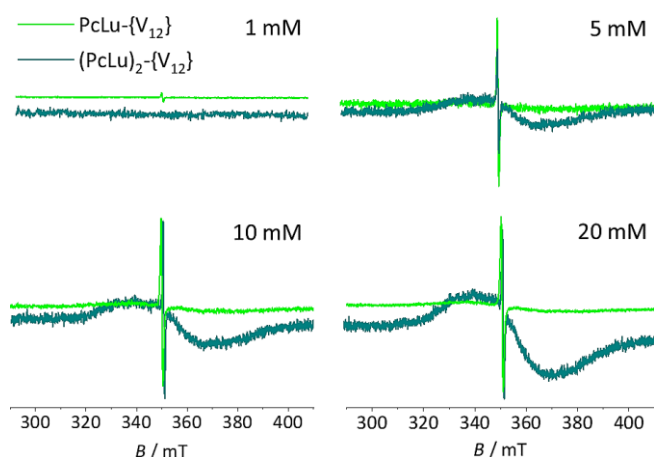

Fig. 5. Solution EPR spectra of PcLu-$\{V_{12}\}$ (green) and (PcLu)$_2$-$\{V_{12}\}$ (dark cyan) at concentrations 1–20 mM measured at r.t. at a frequency of 9.44 GHz, modulation amplitude of 0.1 mT, and microwave power of 0.2 mW.

Computational study

Classical molecular dynamics (MD) and density functional theory (DFT) calculations were carried out for PcLn-$\{V_{12}\}$ and (PcLn)$_2$-$\{V_{12}\}$ compounds to investigate: *i*) their dynamic behaviour in solution at low and high concentrations, *ii*) their electronic structure and the distribution of unpaired electrons in fully-oxidised and one-electron reduced forms, and *iii*) the *intra*- and *inter*molecular electron transfer in the solid state. Understanding the electron mobility both in *intra*- and *inter*molecular fashions is highly relevant for the development of (conducting)[52] molecular quantum materials[53] based on donor–acceptor molecular systems. The following calculations represent the

lower bounds of the real system since they do not include molecular vibrations, which can favour electron hopping processes due to the thermal energy.

MD study

Atomistic MD simulations with explicit solvent molecules were performed to determine the behaviour of PcLn-$\{V_{12}\}$ and (PcLn)$_2$-$\{V_{12}\}$ (for Ln = Lu) in pure CH_2Cl_2 using the GROMACS 5.1.2 code[54,55] and a modified AMBER 99 Force Field,[56] which has been successfully employed in previous studies of the dynamic behaviour of POMs in different environments, including aggregation phenomena.[57–59] The MD trajectories were calculated imposing 3D periodic boundary conditions. Two different fundamental cubic boxes were used: a (8.5 nm)^3 box containing 8 units (PcLn-$\{V_{12}\}$ or (PcLn)$_2$-$\{V_{12}\}$ anions) for the 20 mM (high concentration) solution, and a (11.6 nm)^3 box containing 5 units for the 5 mM (low concentration) solution. Each box contains an appropriate number of nBu_4N^+ counter-cations to ensure the electroneutrality. All simulations were carried out at controlled T = 300 K by coupling the system to a thermal bath using the velocity-rescaling algorithm. Prior to the production runs, all systems were equilibrated by an initial 500 ps run at constant *NVT* fixing the solute, followed by a 500 ps run at constant *NPT* to readjust the box size, and a final 500 ps run at constant *NVT* with relaxed solute. Production trajectories simulate 40 ns with a canonical (*NVT*) ensemble, collecting data every 1 ps. The data from four different MD calculations, 5 mM and 20 mM solutions of PcLn-$\{V_{12}\}$ and (PcLn)$_2$-$\{V_{12}\}$, were analysed with the focus on the mode and the extent of the aggregation between the molecules. The most probable interaction modes are represented in Fig. 6.
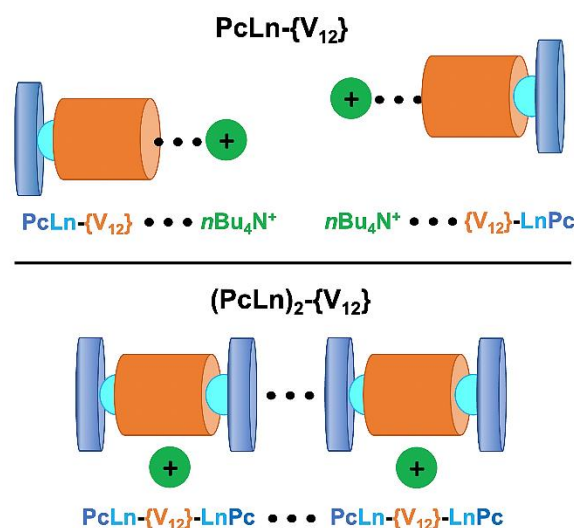

Fig. 6. A schematic representation of preferable modes of *inter*molecular aggregation of dimers in solution in dependence on the number of LnPc ligands present in the respective compound. *Top*: Dimers of PcLn-$\{V_{12}\}$ anions formed by the vertical interaction of two $\{V_{12}\}$ regions with two nBu_4N^+ counter-cations between them. *Bottom*: Dimers of (PcLn)$_2$-$\{V_{12}\}$ anions resulting from the Pc···Pc interactions without nBu_4N^+-mediated aggregation. Not all nBu_4N^+ counter-cations are depicted for the sake of clarity.
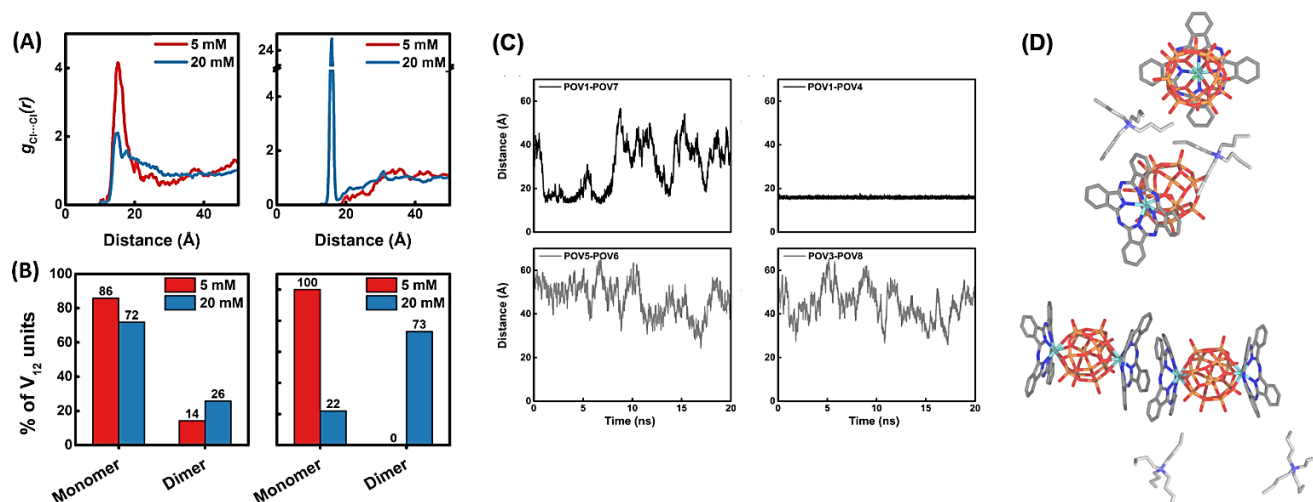
ARTICLE

Fig. 7. Molecular dynamics simulations of the behaviour in solution. (A) Radial distribution functions (RDFs) between Cl centres of {V_{12}} units for PcLn-{V_{12}} (left) and (PcLn)$_2$-{V_{12}} (right), Ln = Lu. Data had been taken every 2 ps from the last 20 ns of MD simulations. (B) State of aggregation, in %, of {V_{12}} units of PcLn-{V_{12}} (left) and (PcLn)$_2$-{V_{12}} (right) compounds. Higher aggregated oligomers (trimers and higher, not displayed) represent less than 1%. (C) Distance vs time evolution of some POV···POV (polyoxovanadate···polyoxovanadate) pairs of PcLn-{V_{12}} (left) and (PcLn)$_2$-{V_{12}} (right) representing different aggregation behaviour. Distances close to 18 Å are considered as dimers. Some pairs form long-lived dimers during the whole trajectory, like POV1···POV4, whereas other pairs remain close for a while and then move away (as in case of POV1···POV7). Some POV units do not show aggregation, as shown in the two cases at the bottom. (D) Representative snapshots of PcLn-{V_{12}} (top) and (PcLn)$_2$-{V_{12}} (bottom), showing the most representative POV···POV interaction mode found. Colour code: V = orange, Cl = green, Ln = turquois, N = blue, C = grey and H = white.

Aggregation of PcLn-{V_{12}} anions (Fig. 6, top) is mediated by nBu$_4$N$^+$ units placed between the two vertically confronted {V_{12}} regions. The anionic nature of the {V_{12}} region keeps nBu$_4$N$^+$ units strongly attached to it *via* Coulomb attraction. Moreover, due to the presence of only one Pc group in PcLn-{V_{12}} anion, the {V_{12}} region is highly exposed to nBu$_4$N$^+$ counter-cations in solution. No long-lived Pc···{V_{12}} contacts were observed (see Fig. 7C, left panels), likely due to their poor mutual electrostatic and dispersive affinity. In contrast, the aggregation of (PcLn)$_2$-{V_{12}} anions can be long-lived (Fig. 7C, right panels) and mostly occurs *via* π–π dispersive interactions between the Pc groups as shown in Fig. 7D (bottom) remarkably with no counter-cation-aided aggregation at all. We suggest that the two bulky Pc groups in (PcLn)$_2$-{V_{12}} units reduce the probability of aggregation *via* the transversally oriented {V_{12}}···{V_{12}} pair, mainly because the nBu$_4$N$^+$ units are not as prone to attach to {V_{12}} as they are in PcLn-{V_{12}}. As mentioned earlier, cation-assisted aggregation of POMs in solution is a well-known phenomenon.[57–59] With the increasing negative charge of the POM, Coulomb interactions become a decisive factor. In the present study, the PcLn-{V_{12}} anion···nBu$_4$N$^+$ interaction, mainly *via* a nBu$_4$N$^+$···{V_{12}} contact, is −912 kJ mol^{-1} *per* unit. This value is much higher than those calculated for the π–π interactions through the Pc···Pc contact (−152 kJ mol^{-1}) and for the less probable (PcLn)$_2$-{V_{12}} anion···nBu$_4$N$^+$ interaction (−135 kJ mol^{-1}) in the (PcLn)$_2$-{V_{12}} compound. In fact, the motions of nBu$_4$N$^+$ and (PcLn)$_2$-{V_{12}} ions in CH$_2$Cl$_2$ solutions are practically uncorrelated.

Next, analysis based on the radial distribution function (RDF or $g(r)$) was performed to determine the concentration-dependent degree of dimer formation, taking into consideration that higher-order aggregates are much less common and ephemeral in time. The RDF is extracted from the averaged structural data of a dynamic system considering two reference points, typically atoms. Fig. 7A shows the Cl···Cl RDF for four runs: diluted (5 mM) and concentrated (20 mM) CH$_2$Cl$_2$ solutions for each PcLn-{V_{12}} and (PcLn)$_2$-{V_{12}} compounds. Upon inspection of the RDFs, we consider formation of a dimer if the distance between two Cl centres is less than the endpoint of the main peak of a RDF, namely 20 Å for PcLn-{V_{12}} and 17.8 Å for (PcLn)$_2$-{V_{12}}. The RDFs for PcLn-{V_{12}} (Fig. 7A) present broad and not well-defined peaks around d(Cl-Cl) = 15 Å, suggesting the prevalence of monomeric units (86% and 77% for 5 and 20 mM, respectively (Fig. 7B, left) over few short-lived dimers in solution. Conversely, the RDF of 20 mM solution of (PcLn)$_2$-{V_{12}} displays a single sharp peak at *ca.* 16 Å, integrating to 0.83 molecules (Fig. 7A, right). In the latter case, the formation of dimers is most preferable in the concentrated solution, accounting for 73% of the species (Fig. 7B, right). In the dilute solution of (PcLn)$_2$-{V_{12}} only monomers were observed.

In summary, the obtained MD simulation data indicate that the structural composition (one or two LnPc ligands *per* {V_{12}} unit) and the concentration of the title nanocomposites determine their supramolecular behaviour which, in turn, impacts their charge transfer characteristics in solution. Based on the experimental results of the concentration dependent EPR measurements (Fig. 5) and the results of the MD calculations, we suggest

that the reduction of the $\{V_{12}\}$ unit in solution takes place through *intra*molecular electron transfer from the Pc group to the $\{V_{12}\}$ core, initiated by sufficiently available *inter*molecular Pc⋯Pc contacts. These π–π dispersive interactions are hardly present, although not completely excludable, in the mono-substituted PcLn-$\{V_{12}\}$ characterised by the predominant degree of $\{V_{12}\}$⋯$\{V_{12}\}$ contacts that are mediated by the counter-cations.

DFT study

We applied the DFT as implemented in ADF2019[60,61] for the study of PcLn-$\{V_{12}\}$ and (PcLn)$_2$-$\{V_{12}\}$ nanocomposites with a combination of the following functionals: OPBE[62] for geometry optimisations and B3LYP[63,64] for the total energies and electronic structures of the equilibrium structures. The hydrogen-free, oxidised mono- and bis-substituted vanadium–oxo clusters were optimised for Ln = Gd (f[7]) and Lu (f[14]). The oxidised and the reduced forms of all Ln[III] derivatives were computed adopting the *closest* reference lanthanide structure (Gd[III] geometry for Ln = Sm[III], Eu[III], Tb[III], Dy[III], and Lu[III] geometry for Ln = Er[III], Yb[III]). Scalar relativistic corrections were introduced by means of the Zeroth-Order Regular Approximation (ZORA).[65–67] Triple-ζ + double polarisation (TZ2P) basis sets with the frozen core approximation (C and N: 1s; Cl: 2s; V: 3p; Ln: 5p) were used. We also computed the metal-free phthalocyanine forms (the neutral (H$_2$Pc) and the deprotonated (Pc^{2-}) forms), the H-free $[V_{12}O_{32}Cl]^{5-}$ POV, and PcLnOAc. We applied the unrestricted formalism to all electronic open-shell systems, except for the oxidised Lu[III]-containing systems, H$_2$Pc and $[V_{12}O_{32}Cl]^{5-}$. Organic solutions were mimicked with the Conductor-like Screening Model (COSMO).[68] We applied Mulliken's formula to obtain the atomic spin densities (ASD).

The fully oxidised $[V_{12}O_{32}Cl]^{5-}$ unit computed in solution, with all V^V metal centres, presents a rather large HOMO–LUMO gap of 3.9 eV. The highest occupied molecular orbital (HOMO) is found at –7.3 eV, with oxo nature, and the lowest unoccupied molecular orbital (LUMO) at –3.4 eV, with vanadium-like nature. If an extra electron is added to the system, it is delocalised equally over 8 vanadium centres. The H$_2$Pc molecule, slightly bent (C_{2v}), is featured by a HOMO–LUMO gap of 2.3 eV, marginally larger than that observed for the planar (D_{4h}) Pc^{2-} (2.1 eV). The calculations in acetonitrile solution resulted in HOMOs at –5.2 eV and –4.4 eV for H$_2$Pc and Pc^{2-}, respectively. Hence, the LUMO of $\{V_{12}\}$ is higher in energy than the HOMO of Pc. The hydrogen-free forms of (PcLn)$_n$-$\{V_{12}\}$, with charges –4 (n = 1) and –3 (n = 2), were computed applying maximal M_s values with all-parallel spins. Frontier orbital energies are shown in Fig. 8 for mono- and bis-substituted Yb[III]-based systems each in the oxidised and the reduced forms. Any mono-substituted system presents a HOMO with Pc nature at *ca.* –4.8 eV, irrespective of Ln, while the LUMO with $\{V_{12}\}$ nature lies 1.1 eV above in all cases (Fig. 9A for a representation of the selected MOs).
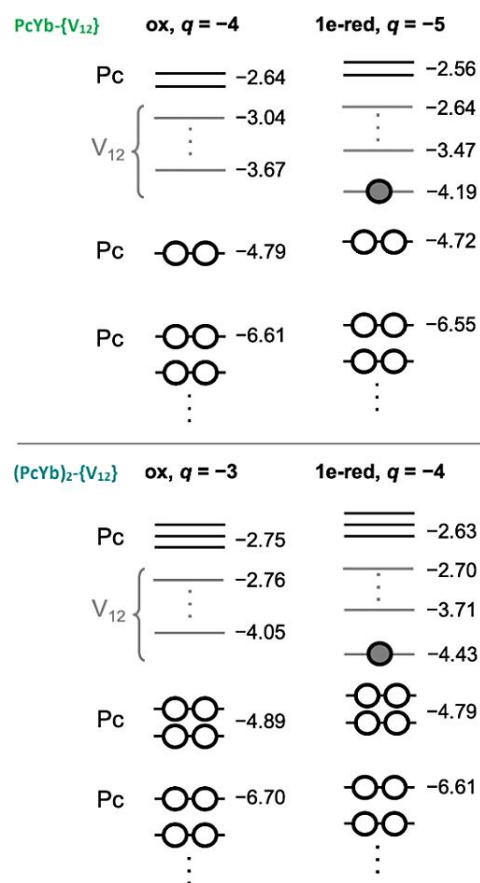

Fig. 8. Sequence of energies and occupations of the frontier MOs, for the mono-substituted PcYb-$\{V_{12}\}$ (top) and the bis-substituted (PcYb)$_2$-$\{V_{12}\}$ (bottom) in their oxidised (ox) and one-electron reduced (1e-red) forms. Counter-cations were not part of these calculations. Circles represent electrons. Values are given in eV.

Table 2. ASD values computed for the mono-substituted PcYb-$\{V_{12}\}$ and the bis-substituted (PcYb)$_2$-$\{V_{12}\}$ each in the oxidised (ox) and one-electron reduced (1e-red) forms. For PcLu-$\{V_{12}\}$, the charge-separated (CS) state ASDs are listed (see also Fig. 9B).

compound	region	ox	1e-red	Lu[III] CS
	Yb	0.995	0.995	0.0
PcLn-$\{V_{12}\}$	$\{V_{12}\}$	0.0	0.294 (×2) 0.282 (×2) 0.148 (×2)	0.295 (×2) 0.282 (×2) 0.146 (×2)
	Pc	0.0	0.0	0.144 (×8)
(PcLn)$_2$-$\{V_{12}\}$	Yb	0.985 (×2)	0.987 (×2)	-
	$\{V_{12}\}$	0.0	0.174 (×8)	-
	Pc	0.0	0.0	-

ASD values obtained for oxidised complexes confirm that the unpaired electrons are fully located on Ln with 6.99 for Gd[III] (f[7]), 6.01 for Eu[III] (f[6]) and 5.00 for Sm[III] (f[5]), whereas other atoms present net zero values.
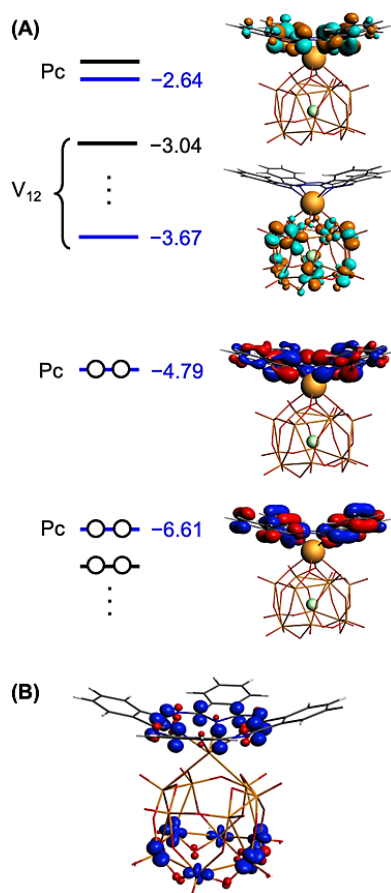
ARTICLE

Fig. 9. DFT analysis of the electronic structure of the mono-substituted PcLn-{V_{12}} compounds. (A) Representation of selected MOs (corresponding to the horizontal blue lines) in the oxidised form of PcYb-{V_{12}}. The character of the orbitals is shown. The rest of the orbitals in the V_{12} block are also vanadium-3d combinations, with the same nature as the orbital depicted. (B) Spin density of the charge-separated species (PcLu)$^{•+}$-{$V^{IV}V^{V}_{11}$}. Blue and red lobes denote regions with the up and down net spin, respectively.

The bis-substituted representatives are featured by similar ASD values for Ln centres. Regarding one-electron reduced systems, when the extra electron added is parallel to the net spin of Ln, in mono-substituted compounds the additional electron occupies the orbital delocalised over six vanadium centres at –4.2 eV (see the ASDs in Table 2), whereas the spin populations of the Ln centres remain unchanged. The behaviour of the bis-substituted derivatives is similar – the additional electron is equally delocalised over eight vanadium centres that participate in the orbital at –4.4 eV. In 1e-reduced systems, when the extra electron located on {V_{12}} is forced to have the opposite spin with respect to that of the Ln centre(s) leads to computed ASD absolute values identical to those of the all spin-up 1e-reduced systems. The energy differences between the all spin-up (HS) and the *spin-flipped* (LS) solutions are usually small, below ~2 cm^{-1} (< 3·10^{-4} eV), except for the mono-substituted Eu^{III}- and Yb^{III}-based systems (with HS ~60 cm^{-1} and ~220 cm^{-1} lower than LS, respectively) and the bis-substituted Dy^{III}-based system (LS is ~13 cm^{-1} lower than HS), suggesting that the net spins in the {V_{12}} and Ln regions are mostly uncoupled.

For the investigation of the *intra*molecular Pc → {V_{12}} electron transfer in mono-substituted PcLn-{V_{12}} compounds, we computed the electronic spectra of Ln = Dy^{III}, Lu^{III} and Gd^{III} to obtain a strong transition involving molecular orbitals of either part of the molecule. Such *intra*molecular electronic transitions, at this level of computation, are described only qualitatively. For each system, we computed the lowest 20 allowed purely electronic transitions. Interestingly, for the Dy^{III}-based system no Pc → {V_{12}} electron transitions were obtained, which roughly corresponds to the experimental observation of one of the weakest V^{IV} signals in EPR for Dy^{III}-containing systems. A weak electron transition in the IR range (1320 nm) was computed for the Lu^{III}-based system, whereas the Gd^{III}-based mono-substituted compound presents the strongest one at *ca.* 620-630 nm with the oscillator strengths *ca.* 100 times larger than for the Lu^{III} analogue. These results suggest that, even not considering the vibronic coupling, there is a non-negligible probability of *intra*molecular electron transfer, at least when Gd^{III} and Lu^{III} are involved. Fig. 9B represents the calculated spin density of the charge-separated mono-(PcLu)$^{•+}$-{$V^{IV}V^{V}_{11}$} which, formally, results from the *intra*molecular charge transfer process.
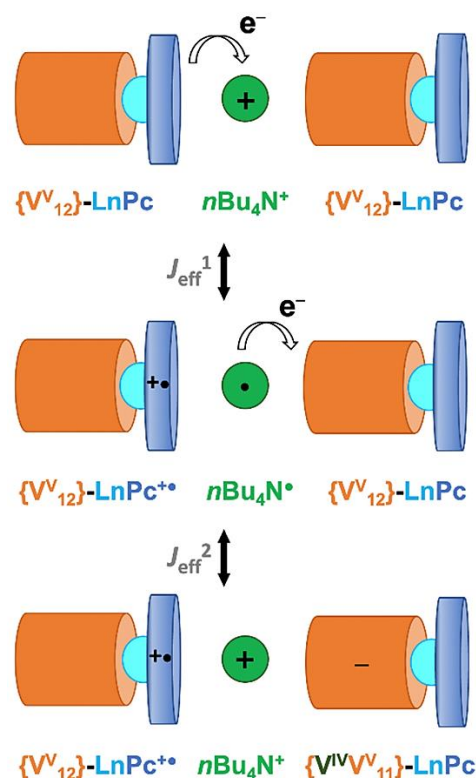

Fig. 10. Counter-cation mediated *inter*molecular electron transport process for mono-PcLn-{V_{12}} compounds, as present at high sample concentrations. Only a section is represented for clarity, not showing additional nBu$_4$N$^+$ counter-cations and H$^+$. The process involves hopping of one electron from a Pc moiety of one PcLn-{V_{12}} anion to the {V_{12}} moiety of another PcLn-{V_{12}} anion, with the nBu$_4$N$^+$ / nBu$_4$N$^•$ pair as a charge mediating platform.

The *inter*molecular electron mobility in PcLn-{V_{12}} and (PcLn)$_2$-{V_{12}} compounds was investigated using the TRANSFERINTEGRALS feature in ADF package.[61] The values reported herein

were obtained from different structural arrangements (crystallographic coordinates, MD snapshots of solution simulations) and single point DFT calculations.
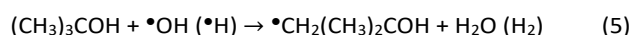
The analysis of the unit cell packing of PcY-$\{V_{12}\}$ leads to the assumption that two electron-hopping pathways are possible, namely one *vertical* and one *transversal*. Ideally, the vertical pathway is a two-step process: 1) the electron transfer from the PcY-$\{V_{12}\}$ anion to nBu$_4$N$^+$ followed by 2) the electron transfer from the resulted formally neutral nBu$_4$N species to another PcY-$\{V_{12}\}$ anion (see Fig. 10). For the vertical electron-hopping pathway we calculated $|J_{eff}^1|$ = 0.0164 eV for the first step and $|J_{eff}^2|$ = 0.0141 eV for the second step. On the other hand, the transversal pathway assumes a direct electron transfer from one PcY-$\{V_{12}\}$ unit to another PcY-$\{V_{12}\}$ without the mediation by counter-cations due to the proximity between two neighbouring units. We computed a very small value of $|J_{eff}|$ = 0.00021 eV, suggesting that the transversal pathway is improbable and, therefore, was not taken into consideration by computing MD arrangements given a rather small impact of aggregation. The electronic structure of the electron deficient mono-[(PcY)$^{\bullet+}$-$\{V_{12}\}$]$^{3-}$ compound, generated upon electron hopping from Pc to a neighbouring molecule, is represented in Fig. S64.

The mechanistic considerations of electron hopping in bis-derivatives made from the analysis of the cell packing in (PcDy)$_2$-$\{V_{12}\}$ are similar to those of mono-substituted analogues. Here, electron transfer takes place from a Pc group of one molecule to the closest nBu$_4$N$^+$ cation, and right away to the next Pc moiety of another molecule involving, again, intercurrent neutral nBu$_4$N$^{\bullet}$ species (Fig. S65). The estimated *effective transfer integrals* of $|J_{eff}^1|$ = 0.00432 eV and $|J_{eff}^2|$ = 0.00446 eV were obtained at the DFT level for Ln = Lu. These are considerably smaller than those for the mono-substituted system and might be attributed *inter alia* to the cell packing differences between the corresponding crystal systems and therewith related proximity of the units to each other. The calculation of a direct *inter*molecular electron hopping, namely without any kind of mediation *via* counter-cations, between the two Pc units for a 20 mM concentrated solution of the bis-derivative resulted in a rather large *effective transfer integral* $|J_{eff}|$ = 0.0136 eV, which roughly explains the experimentally observed strong EPR signal assigned to V^{IV}.

Photo- and radiation chemical study

Further insights into the nanocomposite with the charge-separated (PcLu)$^{\bullet+}$-$\{V^{IV}V^V_{11}\}$ states as suggested by DFT (Fig. 9) were gained by laser photolysis transient absorption spectroscopy. Photo- and radiation chemical studies of the electron donor–acceptor nanocomposites PcLu-$\{V_{12}\}$ and (PcLu)$_2$-$\{V_{12}\}$ as well as the reference compounds $\{V_{12}\}$ and PcLuOAc were conducted in solution to investigate possible photoinduced electron transfer reactions between the photoexcited PcLn group and the $\{V_{12}\}$ cage. With the notion that $\{V_{12}\}$ may act as electron acceptor in PcLu-$\{V_{12}\}$ and (PcLu)$_2$-$\{V_{12}\}$, the one-electron reduction of $\{V_{12}\}$ by solvated electrons in aqueous solutions was probed. Such conditions necessitate the radiolysis of nitrogen saturated dilute aqueous $\{V_{12}\}$ solutions containing 5 vol% *tert*-butanol. The radiolysis of water lead to the production of three highly reactive species, namely $^{\bullet}$H, $^{\bullet}$OH, and e$_{aq}^-$ (equation (4)), besides the molecular products H$_2$ and H$_2$O$_2$.[69] The function of t-butanol is to efficiently scavenge two of the radical species, namely $^{\bullet}$H and $^{\bullet}$OH, via hydrogen abstraction (equation (5))[69] so that only e$_{aq}^-$ – a very strong reducing intermediate[70] – remains as reactive species to react with $\{V_{12}\}$, forming the one-electron reduced form of the $\{V_{12}\}$ (equation (6)).

$$H_2O \rightsquigarrow e^-_{aq} + {}^{\bullet}H + {}^{\bullet}OH \tag{4}$$

$$(CH_3)_3COH + {}^{\bullet}OH \,({}^{\bullet}H) \rightarrow {}^{\bullet}CH_2(CH_3)_2COH + H_2O \,(H_2) \tag{5}$$

$$\{V_{12}\} + e_{aq}^- \rightarrow \quad \{V_{12}\}^- \tag{6}$$

Immediately after the radiation pulse, a well-established broad transient absorption of e$_{aq}^-$ with its maximum at around 720 nm was recorded, which decayed rapidly in the presence of $\{V_{12}\}$ giving rise to a new transient throughout the UV and visible part of the optical spectrum. Features of the resulting absorption spectrum (Fig. S66) include a maximum at 350 nm and a minimum at 310 nm which can be assigned to the one-electron reduced $\{V^{IV}V^V_{11}\}$ cage. The rate constant for the reaction of the fully-oxidised $\{V^V_{12}\}$ with e$_{aq}^-$ was determined from the decay of the transient absorption of e$_{aq}^-$ at 720 nm at different $\{V_{12}\}$ concentrations (Fig. S66) assuming a pseudo-first-order kinetic. In this way a bimolecular rate constant with the value of 5×10^9 M^{-1}s^{-1} was obtained. With the transient absorption spectrum of the one-electron reduced $\{V^{IV}V^V_{11}\}$ on hands, photophysical studies of PcLuOAc, PcLu-$\{V_{12}\}$ and (PcLu)$_2$-$\{V_{12}\}$ were conducted.

The electronic ground state absorption spectrum of PcLuOAc exhibits a set of Q-bands, an intense absorption maximum at around 673 nm preceded by a minor maximum at around 610 nm. Additionally, B-band (the Soret-bands) absorptions of the Pc macrocycle are observed at around 342 nm (Fig. 11). The observation of the Q- and B-band absorptions are in line with the plethora of the published absorption spectra typical for metal phthalocyanines.[71,72]
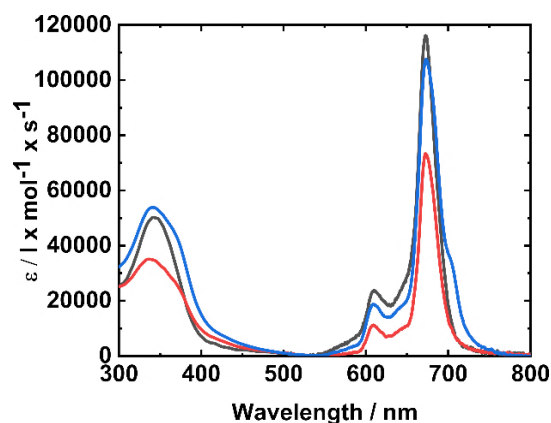

Fig. 11. Absorption spectra of PcLuOAc in toluene (black), PcLu-$\{V_{12}\}$ in THF (red) and (PcLu)$_2$-$\{V_{12}\}$ in THF (blue).

ARTICLE

Upon the comparison of the electronic ground state absorptions of the electron donor–acceptor PcLu-{V$_{12}$} and (PcLu)$_2$-{V$_{12}$} with that of PcLuOAc, the two nanocomposites can be qualitatively described as the sum of the absorption spectra of PcLuOAc and {V$_{12}$}. In particular, strong Q-bands with absorption maxima at around 673 nm and 609 nm accompanied by the B-band absorptions with maxima at 335 nm (PcLu-{V$_{12}$}) and 339 nm ((PcLu)$_2$-{V$_{12}$}) based on the phthalocyanine-centred transitions were observed (Fig. 11). Interestingly, the absorption spectrum of (PcLu)$_2$-{V$_{12}$} shows a shoulder at the low energy edge of the Q-band absorption around 710 nm. The nature of the shoulder may relate to a charge transfer band, on the one hand;[73] on the other, the formation of aggregates showing similar spectroscopic features cannot be excluded either.[74,75] The lower extinction coefficients of the Q-band for PcLu-{V$_{12}$} and (PcLn)$_2$-{V$_{12}$} compared to PcLuOAc may indicate electronic communication between the PcLu and {V$_{12}$} moieties in the ground state, which was previously observed for different porphyrinoid-based electron donor–acceptor systems.[76–78] The B-band absorptions of PcLu-{V$_{12}$} and (PcLu)$_2$-{V$_{12}$} appear somewhat broader than that observed for PcLuOAc and the maxima are slightly shifted towards the UV area. The most feasible rationale for this finding is that the UV absorption of PcLu-{V$_{12}$} and (PcLu)$_2$-{V$_{12}$} can be described as an overlap of the B-band absorption of the phthalocyanine macrocycle with the absorption spectrum of {V$_{12}$}; the latter is characterised by the absorption mainly in the UV region of the optical spectrum with a maximum at around 232 nm and a shoulder at around 340 nm (Fig. S67).

The excited state properties of PcLuOAc, PcLu-{V$_{12}$} and (PcLu)$_2$-{V$_{12}$} were studied by fluorescence and nanosecond laser photolysis transient absorption spectroscopy. LuPcOAc in toluene, PcLu-{V$_{12}$} and (PcLu)$_2$-{V$_{12}$}, both in tetrahydrofuran (THF), exhibit only marginal fluorescence with maxima at around 680, 672 and 673 nm (Fig. S68) and quantum yields of 0.0035, 0.0032 and 0.0027, respectively.[§] In line with the very low fluorescence quantum yields, fluorescence lifetime measurements for all three compounds revealed lifetimes below the resolution of our TCSPC setup (below 100 ps) indicating that the first excited singlet state lifetime for PcLuOAc, PcLu-{V$_{12}$} and (PcLu)$_2$-{V$_{12}$} lay below 100 ps.

The transient absorption signature of the first excited triplet state of PcLuOAc was established by means of the nanosecond laser photolysis. It consists of a broad transient absorption maximum at around 490 nm accompanied by transient absorption minima at 340, 610 and 670 nm mirror-imaging the B- and Q-bands of the ground state absorption (Fig. S69). This transient absorption is in line with previously reported transition absorptions of the T$_1$ state of phthalocyanine macrocycles.[71,79,80] To shed light on a possibly formed charge-separated state in (PcLu)$^{\bullet+}$-{V^{IV}V$^V_{11}$} and (PcLu)$_2$$^{\bullet+}$-{V^{IV}V$^V_{11}$}, nanosecond-resolved transient absorption spectroscopy was employed. Hereby, PcLu-{V$_{12}$} and (PcLu)$_2$-{V$_{12}$} were probed in THF upon photoexcitation at 355 nm.

The transient absorption spectrum (Fig. 12) obtained from PcLu-{V$_{12}$} shows absorption bands throughout the visible and NIR part of the optical spectrum with a broad maximum at around 550 nm and a rather narrow maximum at around 830 nm. Such transient absorptions, in particular the transient absorption maximum around 830 nm, is diagnostic for one electron oxidised phthalocyanine radical cations,[81–84] giving strong evidence for the envisioned electron transfer from the photoexcited PcLu ligand to the {V$_{12}$} cage in PcLu-{V$_{12}$}. Fitting the decay at 830 nm (Fig. 12, inset) with a monoexponential decay function resulted in lifetimes for the (PcLu)$^{\bullet+}$-{V^{IV}V$^V_{11}$} state of around 170 ns, which is rather long lived taking the close proximity of the electron donor and acceptor into account. For (PcLu)$_2$-{V$_{12}$} the obtained transient absorption spectrum differs considerably from that of PcLu-{V$_{12}$}. Photoexcitation of (PcLu)$_2$-{V$_{12}$} in THF with nanosecond laser pulse at 355 nm resulted in strong transient absorptions throughout the UV and a visible part of the optical spectrum with maxima at around 620 and 830 nm and a minimum at around 690 nm. This transient absorption decayed rather rapidly with a lifetime of around 40 ns (Fig. S70). The observed transient absorption resembles neither the transient absorption spectrum of the T$_1$ state of PcLuOAc nor the commonly seen transient absorption signatures of the one electron oxidised phthalocyanine macrocycles. This observation can probably be explained by the fact that in (PcLu)$_2$-{V$_{12}$} the {V$_{12}$} unit is sandwiched between the two PcLu fragments, and therefore, an electron transfer to {V$_{12}$} may result in a distribution of the positive charge between both PcLu moieties, thus leading to a transient absorption spectrum not fitting with the absorption spectrum of a one-electron oxidised Pc macrocycle.
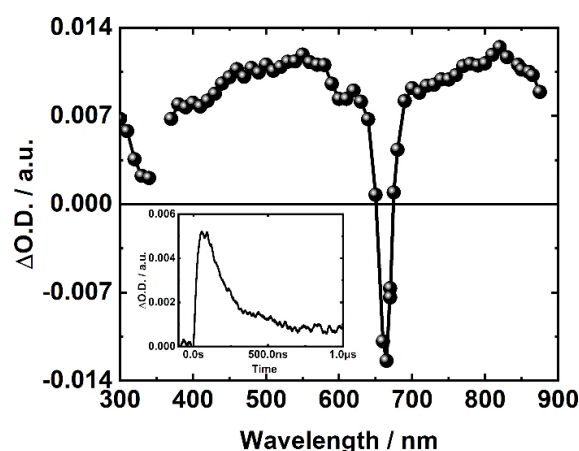

Fig. 12. Nanosecond laser photolysis transient absorption spectrum of PcLu-{V$_{12}$} in N$_2$ saturated THF 150 ns after excitation at 355 nm (5 ns FWHM, 5 mJ/pulse). Inset: Corresponding time absorption profiles at 830 nm.

Magnetism and magnetochemical modelling

To gain preliminary insights into the opportunities to utilise the synthesised molecular nanocomposites with Ln = Sm^{III}–Er^{III} and Lu^{III} as information storage,[85–88] we measured AC susceptibility. Only the Dy^{III}-containing mono- and bis-derivatives revealed

some non-zero out-of-phase signal. In the following magneto-chemical studies we focus exclusively on the PcDy-{V$_{12}$} derivative as it has the strongest AC magnetism.

Both DC and AC measurements have been performed by the standard SQUID technique (B = 0–7.0 T and T = 2.0–300.0 K, f = 1–1200 Hz, for further details of the measurements refer to the ESI†). The EPR (Fig. 4) revealed that the magnetism of PcDy-{V$_{12}$} is induced not only by Dy^{III} but also by an electron delocalised over {V$_{12}$}. However, DFT results exclude a possibility of an electron transition from Pc to {V$_{12}$}. Thus, it seems that in this compound we observe *inter*molecular charge transfer from Pc to {V$_{12}$} (*via* counter-cations) resulting in two configurations: one-electron reduced (Fig. 8) and electron deficient (Fig. S64). The latter one cannot be detected by room temperature EPR.[40] In both configurations there is an extra electron that can interact with Dy^{III}. Therefore, under the assumption that below room temperature only the ground multiplet arising from spin-orbit coupling (in Dy^{III}) is relevant, the DC magnetic measurements can be modelled by the following Hamiltonian (equation (1)):

$$H = -\mu_B\big[g_\perp\big(J_xB_x + J_yB_y\big) + g_\parallel J_zB_z + g\boldsymbol{S}\cdot\boldsymbol{B}\big]$$
$$+ K\boldsymbol{S}\cdot\boldsymbol{J} + DJ_z^2 + E\big(J_x^2 - J_y^2\big), \tag{1}$$

where $\boldsymbol{J} = (J_x, J_y, J_z)$ (J = 15/2) is the total angular momentum of Dy^{III} and $\boldsymbol{S}$ is the spin ½ of an electron delocalised over some ions at {V$_{12}$}, or at Pc. The last two terms account for the interaction of $\boldsymbol{J}$ with the crystal field. The z-axis goes through Cl$^-$ and Dy^{III} ions. First, we assumed that $E = 0$. Then, the best fit (fit a) has been obtained for $g_\perp = 1.30$, $g_\parallel = 1.34$, $K/k_B = 1.7\,K$, $D/k_B = -12.2\,K$ (Fig. 13). Since the fitted g values are very close to the free ion $g = 4/3$ one can eliminate g from the fitting by fixing it to the free ion value and obtain very similar unique values of D and K (Fig. S71). Yet, the introduction of small anisotropy in g allows to fine tune the fit in high temperatures. Moreover, it can be demonstrated that a condition $K \neq 0$ is indispensable to obtain a good fit and cannot be substituted by more crystal field terms (Fig. S71), which clearly indicates existence of the interaction between Dy^{III} and the radical electron. (see the ESI† for the detailed DC modelling). The observed room temperature χT was found to be $1.78\cdot10^{-4}$ m^3 mol^{-1}, which is within the range for a theoretical value of $1.77\cdot10^{-4}$ m^3 mol^{-1} for a free Dy^{III} ion and $1.81\cdot10^{-4}$ m^3 mol^{-1} when an additional electron is considered. A weak antiferromagnetic interaction $K/k_B = 1.7\,K$ between the Dy^{III} ion and the unpaired electron is stronger than the above DFT estimate (< 0.46 K). It can be due to the fact that the DFT estimate is only true for the interaction between Dy^{III} and {V$_{12}$}-delocalised electron whereas the value obtained from the fitting is an average of interaction of Dy^{III} with Pc- and {V$_{12}$}-located electrons. The negative D value suggests the existence of an energy barrier in the Orbach relaxation process estimated to be around 686 K. However, in the absence of the static field the AC out-of-phase signal at temperatures below 10 K shows no clear peaks in the available frequency range.

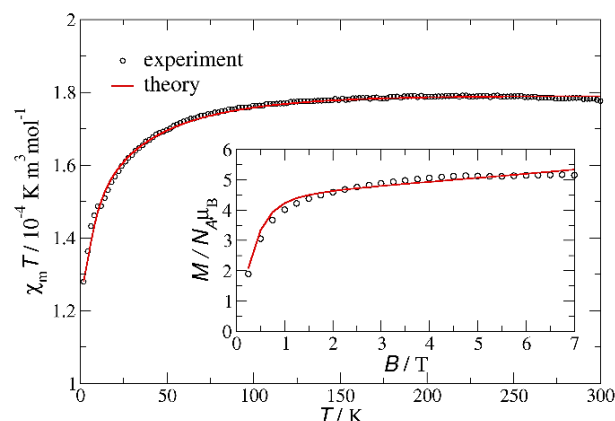This points out a fast relaxation through quantum tunnelling of magnetisation (QTM).[89,90]

Fig. 13. Molar susceptibility (B = 0.1 T) and magnetisation (T = 2 K) for PcDy-{V$_{12}$} (black circles) with theoretical fits assuming E = 0 (solid red lines).

When the static field is applied the AC out-of-phase signal exhibits clear peaks. Using standard methods[91] (see also the ESI†) we extracted the relaxation time from measurements made at T = 2 K for different static fields B. The best fit for the relaxation rate τ^{-1} versus B was obtained with the equation (2) considering QTM and direct paths of relaxation[92] (Fig. 14):

$$\tau^{-1} = \frac{b_1}{1 + b_2 B^2} + aTB^n, \tag{2}$$

with the following parameters: b_1 = 17133 ± 2765 1/s, b_2 = 1695 ±302 1/T^2, a = 32296 ±22235 T^{-n}/Ks, n = 5.08 ±0.6 and B in Tesla. The uncertainties (given after ±) define 95% confidence intervals. For B = 0 the relaxation rate of PcDy-{V$_{12}$} has a divergent error bar (with the upper limit against the infinity) indicating that the relaxation time cannot be measured with the current method.
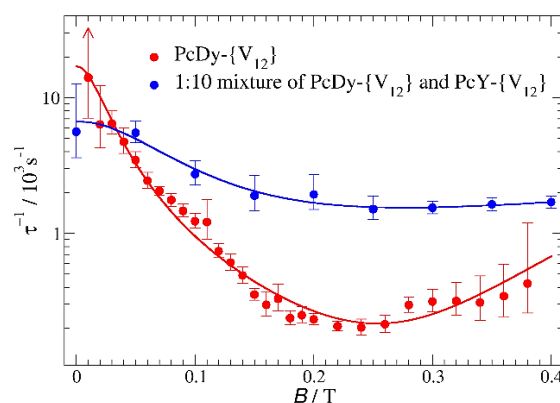

Fig. 14. Relaxation rate for different values of the static field B at T = 2 K obtained for PcDy-{V$_{12}$}. The fitting has been performed based on the formula (2). The error bars mark 95% confidence intervals.

ARTICLE

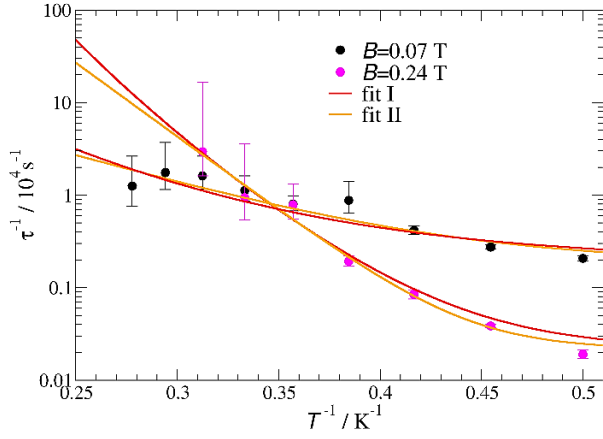
Fig. 15. Temperature dependence of relaxation rate for static field B = 0.07 T and B = 0.24 T in PcDy-{V$_{12}$}. The error bars mark 95% confidence intervals.

Temperature dependent measurements were performed for B = 0.07 T and B = 0.24 T, for which the strongest out-of-phase signal and the longest relaxation time (at T = 2 K) were found, respectively (Figs. S72-S78). In Fig. 15 the relaxation rate is plotted versus temperature. For temperatures higher than 3.6 K the relaxation time is too short and cannot be detected with a standard AC magnetometry. The following two approaches gave equally good results: I) fitting the data with QTM, direct and Raman processes (the first three terms in equation (3)), and II) fitting the data with QTM, direct and Orbach processes (the first, second and fourth term in equation (3)):

$$\tau^{-1} = \tau_{QTM}^{-1} + aTB^n + CT^m + \exp\left(-\frac{E_{eff}}{T}\right)/\tau_0, \qquad (3)$$

where τ_{QTM}^{-1} is the first term in formula (2) calculated for the given field.

Table 3. Fitted parameters in equation (3) and their 95% confidence intervals (in square brackets). Confidence intervals are due to error bars of τ^{-1} and to uncertainties of τ_{QTM}^{-1}, a and n obtained from the fit of formula (2).

fit	parameters	B = 0.07 T	B = 0.24 T
I	C / sK^{-m}	23.1 [4.4, 53.5]	0.012 [0.003, 0.02]
	m	5.16 [4.5, 6.4]	12.64 [12.1, 13.7]
II	E_{eff} / K	14.5 [12.6, 18]	36.8 [34.6, 39.4]
	τ_0 / 10^{-6}s	1 [0.52, 1.6]	3.7 [2.2, 5.2] · 10^{-4}

Parameters a and n attain the values according to equation (2). For B = 0.07 T a direct process has negligible contribution to τ^{-1} and is omitted in fitting. The remaining parameters in (3) are obtained from the fitting of τ^{-1} versus T and are shown in Table 3. Attempts to fit τ^{-1} versus T with the formula containing QTM, Raman, and Orbach processes simultaneously or in other combinations were unsuccessful. In Kramers doublet systems like Dy^{III} QTM is formally forbidden.[93] However, in real systems the time reversal symmetry is often broken by the transverse local magnetic fields resulting from the dipole magnetic interaction with other magnetic molecules[94] or the interaction with magnetically active nuclei[95] thus opening a tunnel splitting. The

transverse crystal field can influence the size of a tunnelling gap.[96] In the case of the PcDy-{V$_{12}$} compound there is additionally an interaction with the unpaired electron delocalised over {V$_{12}$} cluster. All these factors may play a role in encouraging relaxation through QTM.

To verify the impact of the magnetic dipole interactions between Dy^{III} ions we determined the relaxation rate in 1:10 mixture of PcDy-{V$_{12}$} and PcY-{V$_{12}$} (Fig. 13) at T = 2 K. As Y^{III} is diamagnetic, the distance between Dy^{III} ions and thus the strength of magnetic dipole interactions should decrease. Indeed, at B = 0 the relaxation rate assumes a finite value. Yet, the relaxation time at B = 0 is still short suggesting that other factors can also play a role. It can be shown, for instance, that the strength of the magnetic dipole interaction between Dy^{III} ion and an electron at {V$_{12}$} is of the same order as the strength of the same interaction between Dy^{III} ions (see the ESI†).
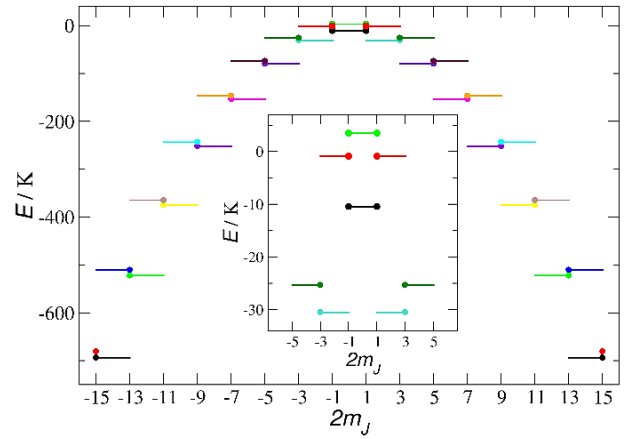

Fig. 16. Energy spectrum of PcDy-{V$_{12}$} for static field B = 0. The lines marking energy levels extend over m_J represented in an eigenstate. Circles mark dominant components and the states from the same doublet are plotted with the same colour.

The energy spectrum of Hamiltonian (1) with optimal parameters is presented in Fig. 16. The eigenstates have a form of a superposition of states $|m_J\rangle|m_S\rangle$, where m_J and m_S stand for the projections of $\boldsymbol{J}$ and $\boldsymbol{S}$, respectively. The lines marking the energy levels in Fig. 16 extend over the values of m_J (labelled at the horizontal axis) which correspond to the components $|m_J\rangle$ presented in a superposition forming a given eigenstate. Obviously, the interaction with the unpaired electron at {V$_{12}$} leads to the splitting of all energy levels and the superposition of the states with different projections m_J. The energy gap between the ground and the first excited states is equal to 13.1 K (13.8 K, if magnetic dipolar interactions are considered), which fits well to the effective energy barrier obtained from the fitting of the QTM, and Orbach processes (12.6–18. K) for B = 0.07 T. This may indicate that for B = 0.07 T the thermally assisted QTM process takes place through the first excited state, which will favour the fit II. For B = 0.24 T it is difficult to find a correspondence between the energy spectrum and the effective energy (34.6–39.4 K) obtained from the fit II. This may be caused by a large magnitude of the external magnetic field, which hinders the thermally assisted QTM through the first excited state. Therefore, in this

case the fit I, which considers a Raman process, should be favoured. When the magnetic dipolar interaction between Dy^{III} ion and the electron at $\{V_{12}\}$ is included in Hamiltonian (1) the optimal parameters are slightly different and the energy spectrum looks very much the same as that presented in Fig. 16 with the major differences being that the doublets are not degenerated anymore, and the eigenstates contain a superposition of states with all possible m_J. The tunnel splitting is equal to $1.26 \cdot 10^{-8}$ K for the lowest doublet and $1.6 \cdot 10^{-6}$ K for the first excited doublet.

In principle, these results support the idea of QTM through the ground and first excited states. However, in the low lying states the superposition of terms with opposite values of m_J is very small. For instance, in the ground doublet the dominant component corresponding to $m_J = -15/2$ or $15/2$ has a 99.97% share in the eigenstate. Thus, a direct tunnelling between these states is unlikely and there must be another mechanism that introduces larger superposition of states with opposite m_J. Such a superposition can be induced by e.g., transverse crystal field terms. To test this possibility, we introduced to the Hamiltonian (1) the lowest order transverse crystal field term. Since $g_\perp$ and $g_\parallel$ from the optimal fit (fit a) are very close to each other we fix $g_\perp = g_\parallel$. Then, starting from the optimal fit a, we found an almost equally good fit (fit b) with nonzero value of E: $g_\perp = g_\parallel = 1.33$, $K/k_B = 1.6$ K, $D/k_B = -9$ K, $E/k_B = 2.6$ K. The low-lying energy spectrum is very similar to that in fit a, but there is a large superposition of the terms with the opposite values of m_J. For example, the contributions of the terms with $m_J = 15/2$ and $m_J = -15/2$ in the split ground doublet are approximately equal to 49%. The tunnel splitting is equal to $1.6 \cdot 10^{-4}$ K for the ground doublet and $3.2 \cdot 10^{-5}$ K for the first excited doublet. Of course, the fitting of susceptibility does not enable us to determine more than a leading crystal field term. Therefore, fit b should be considered only as a proof of concept.

Thus, it can be concluded that the pure QTM relaxation at 2 K is probably enhanced at higher temperatures by thermally assisted QTM (for smaller magnetic fields) or Raman processes (for larger magnetic fields). The QTM cannot be completely quenched by dilution with non-magnetic molecules because tunnel splitting of doublets is caused also by the magnetic dipolar interaction between Dy^{III} ion and an electron at $\{V_{12}\}$ or Pc and probably also enhanced by transverse crystal field terms.

Conclusions

We successfully synthesised and fully characterised a series of mono- and bis-functionalised nanocomposites PcLn-$\{V_{12}\}$ and (PcLn)$_2$-$\{V_{12}\}$, respectively. Solution and solid state EPR revealed that proximity of the molecules generates reduced V(3d) states in the closely packed $\{V_{12}O_{32}\}$ cages. As corroborated by a combined experimental and computational approach this effect can be assigned to two processes:

1) a non-photoinduced *intra*molecular electron transfer from the electron-donating LnPc moiety to the electron-accepting redox-active $\{V_{12}O_{32}\}$ building block of the nanocomposite with the resulting charge-separated states (PcLn)$^{\bullet+}$-$\{V^{IV}V^V_{11}\}$. This process can be exemplified in Lu-based mono compound, where a radical electron located also at Pc is confirmed by r.t. EPR. The existence of the charge-separated state is confirmed by laser photolysis transient absorption spectroscopy. DFT calculations provide a nonzero probability of the electron transition from Pc to $\{V_{12}\}$. *Intra*molecular charge transfer seems to be excluded for the Dy-based mono compound as no Pc $\rightarrow \{V_{12}\}$ transitions were found in the framework of DFT approach.

2) a counter-cation-mediated *inter*molecular electron transfer from Pc of one molecule to $\{V_{12}\}$ of another molecule. As a result of this process, two states are generated: one-electron reduced, and electron deficient which give rise to an unpaired electron at $\{V_{12}\}$ and at Pc, respectively. The latter state cannot be detected by r.t. EPR if Ln is paramagnetic, but its existence can be inferred from the fact that Pc is the most probable donor in this system. The existence of this process is confirmed by DFT and MD.

AC-magnetometry revealed that Dy-based compounds are field induced single molecule magnets with the mono compound giving the strongest out-of-phase signal. Measurements of a diluted sample for mono compound and theoretical calculations imply that the relaxation process at low temperature is dominated by the quantum tunnelling induced by magnetic dipolar interactions between Dy^{III} ions as well as between a Dy^{III} ion and an unpaired electron delocalised over the $\{V_{12}O_{32}\}$ core or Pc. Magnetochemical modelling of the PcDy-$\{V_{12}\}$ indicates that there is a weak antiferromagnetic interaction between Dy^{III} and unpaired electron located at Pc or $\{V_{12}\}$, which is consistent with DFT results.

The obtained results persuade us to further research this type of responsive nanocomposites with the far-reaching goal of their future implementation into molecularly powered classic and quantum sensor / computing technologies.[97] The challenging goals here are (1) to generate entanglement between two magnetic states (of delocalised electron and Ln) e.g. by means of electric field[98], (2) to reveal the effect[99] of external magnetic field on the lifetime of charge-separated states, and (3) to incorporate functional PcLn-$\{V_{12}\}$ and (PcLn)$_2$-$\{V_{12}\}$ as active switching components into highly ordered two- or three-dimensional porous frameworks.

We are currently performing large-area electron transport measurements of the title nanocomposites on suitable substrate surfaces, which will be reported elsewhere. The latter studies should provide answers to the effect of an external electric field[100] on the magnetic state of an entire molecular nanocomposite resulting between other from moving the delocalised electron in or out of the exchange contact with Ln.

Author Contributions

I.W., X.L., P.K., A.K. and K.Y.M. co-wrote the manuscript. I.W. performed synthesis, spectroscopic data analysis and electrochemical study. J.G. conducted EPR spectroscopy. A.M.-S. and X.L. performed computational study. K.Z. carried out DC and AC SQUID measure-

ARTICLE

Conflicts of interest

There are no conflicts to declare.

Acknowledgements

Notes and references

§ The fluorescence quantum yields should be considered as the upper limit, since already marginal residual amounts (< 0.1%) of free base phthalocyanines from the syntheses may contribute substantially to the observed fluorescence.

1. M. T. Pope and U. Kortz, In *Encyclopedia of Inorganic and Bioinorganic Chemistry*, ed. R. A. Scott, John Wiley & Sons, Ltd., Chichester, 2012.
2. D.-L. Long, R. Tsunashima and L. Cronin, *Angew. Chem., Int. Ed.*, 2010, **49**, 1736.
3. A. Misra, K. Kozma, C. Streb and M. Nyman, *Angew. Chem., Int. Ed.*, 2020, **59**, 596.
4. N. I. Gumerova and A. Rompel, *Chem. Soc. Rev.*, 2020, **49**, 7568.
5. J. M. Cameron, G. Guillemot, T. Galambos, S. S. Amin, E. Hampson, K. Mall Haidaraly, G. N. Newton and G. Izzet, *Chem. Soc. Rev.*, 2022, **51**, 293.
6. A. V. Anyushin, A. Kondinski and T. N. Parac-Vogt, *Chem. Soc. Rev.*, 2020, **49**, 382.
7. G. Izzet, F. Volatron and A. Proust, *Chem. Rec.*, 2017, **17**, 250.
8. S. Sanvito, *Chem. Soc. Rev.*, 2011, **40**, 3336.
9. A. Forment-Aliaga and E. Coronado, *Chem. Rec.*, 2018, **18**, 737.
10. M. Stuckart and K. Y. Monakhov, *Chem. Sci.*, 2019, **10**, 4364.
11. N. I. Gumerova and A. Rompel, *Nat. Rev. Chem.*, 2018, **2**, 0112.
12. J. Dreiser, *J. Phys.: Condens. Matter*, 2015, **27**, 183203.
13. a) C. Ritchie and C. Boskovic, In *Polyoxometalate Chemistry Some Recent Trends*, ed. F. Sécheresse, World Scientific, Singapore, 2013, p. 177-214; b) M. Vonci and C. Boskovic, *Aust. J. Chem.*, 2014, **67**, 1542; c) C. Ritchie, V. Baslon, E. G. Moore, C. Reber and C. Boskovic, *Inorg. Chem.* 2012, **51**, 1142.
14. C. Costa-Coquelard, S. Sorgues and L. Ruhlmann, *J. Phys. Chem. A*, 2010, **114**, 6394.
15. I. Ahmed, R. Farha, M. Goldmann and L. Ruhlmann, *Chem. Commun.*, 2013, **49**, 496.
16. K. Pamin, M. Prończuk, S. Basąg, W. Kubiak, Z. Sojka and J. Połtowicz, *Inorg. Chem. Commun.*, 2015, **59**, 13.
17. A. Panagiotopoulos, A. M. Douvas, P. Argitis and A. G. Coutsolelos, *ChemSusChem*, 2016, **9**, 3213.
18. M. Natali, E. Deponti, D. Vilona, A. Sartorel, M. Bonchio and F. Scandola, *Eur. J. Inorg. Chem.*, 2015, 3467.
19. Y. F. Song and R. Tsunashima, *Chem. Soc. Rev.*, 2012, **41**, 7384.
20. I. Radivojevic, K. Ithisuphalap, B. P. Burton-Pye, R. Saleh, L. C. Francesconi and C. M. Drain, *RSC Adv.*, 2013, **3**, 2174.
21. S. Sarwar, S. Sanz, J. van Leusen, G. S. Nichol, E. K. Brechin and P. Kögerler, *Dalton Trans.*, 2020, **49**, 16638.
22. O. Linnenberg, M. Moors, A. Notario-Estévez, X. López, C. de Graaf, S. Peter, C. Baeumer, R. Waser and K. Y. Monakhov, *J. Am. Chem. Soc.*, 2018, **140**, 16635.
23. M. Stuckart, N. V. Izarova, M. Glöß, J. Klose, C. Schmitz-Antoniak, P. Kögerler, B. Kersting and K. Y. Monakhov, *Inorg. Chem.*, 2021, **60**, 8437.
24. K. Y. Monakhov, W. Bensch and P. Kögerler, *Chem. Soc. Rev.*, 2015, **44**, 8443.
25. M. Stuckart and K. Y. Monakhov, In *Encyclopedia of Inorganic and Bioinorganic Chemistry*, ed. R. A. Scott, John Wiley & Sons, Ltd., Chichester, 2018.
26. R. Putt, P. Kozłowski, I. Werner, J. Griebel, S. Schmitz, J. Warneke and K. Y. Monakhov, *Inorg. Chem.*, 2021, **60**, 80.
27. R. Putt, X. Qiu, P. Kozłowski, H. Gildenast, O. Linnenberg, S. Zahn, R. C. Chiechi and K. Y. Monakhov, *Chem. Commun.*, 2019, **55**, 13554.
28. K. Okaya, T. Kobayashi, Y. Koyama, Y. Hayashi and K. Isobe, *Eur. J. Inorg. Chem.*, 2009, **2009**, 5156.
29. K. Kastner, J. Forster, H. Ida, G. N. Newton, H. Oshio and C. Streb, *Chem. Eur. J.*, 2015, **21**, 7686.
30. K. Kastner, M. Lechner, S. Weber and C. Streb, *ChemistrySelect*, 2017, **2**, 5542.
31. M. H. Anjass, K. Kastner, F. Nagele, M. Ringenberg, J. F. Boas, J. Zhang, A. M. Bond, T. Jacob and C. Streb, *Angew. Chem., Int. Ed.*, 2017, **56**, 14749.
32. A. Seliverstov and C. Streb, *Chem. Eur. J.*, 2014, **20**, 9733.
33. J. M. Cameron, G. N. Newton, C. Busche, D. L. Long, H. Oshio and L. Cronin, *Chem. Commun.*, 2013, **49**, 3395.
34. M. Šimuneková, D. Prodius, V. Mereacre, P. Schwendt, C. Turta, M. Bettinelli, A. Speghini, Y. Lan, C. E. Anson and A. K. Powell, *RSC Adv.*, 2013, **3**, 6299.
35. B. Schwarz, M. Durr, K. Kastner, N. Heber, I. Ivanovic-Burmazovic and C. Streb, *Inorg. Chem.*, 2019, **58**, 11684.
36. S. Greiner, B. Schwarz, M. Ringenberg, M. Durr, I. Ivanovic-Burmazovic, M. Fichtner, M. Anjass and C. Streb, *Chem. Sci.*, 2020, **11**, 4450.
37. S. Greiner, B. Schwarz, C. Streb and M. Anjass, *Chem. Eur. J.*, 2021, **27**, 1.
38. J. J. Chen, M. D. Symes and L. Cronin, *Nat. Chem.*, 2018, **10**, 1042.
39. M. Bouvet, P. Bassoul and J. Simon, *Mol. Cryst. Liq. Cryst.*, 1994, **252**, 31.
40. K. L. Trojan, W. E. Hatfield, K. D. Kepler and M. L. Kirk, *J. Appl. Phys.*, 1991, **69**, 6007.
41. F. H. Winslow, W. O. Baker and W. A. Yager, *J. Am. Chem. Soc.*, 1955, **77**, 4751.
42. G. P. Eyer, K. R. Kittilstved and T. L. Andrew, *J. Phys. Chem. C*, 2017, **121**, 24929.

43. K. Y. Monakhov, O. Linnenberg, P. Kozłowski, J. van Leusen, C. Besson, T. Secker, A. Ellern, X. López, J. M. Poblet and P. Kögerler, *Chem. Eur. J.*, 2015, **21**, 2387.

44. A. Müller, M. T. Pope, A. M. Todea, H. Bogge, J. van Slageren, M. Dressel, P. Gouzerh, R. Thouvenot, B. Tsukerblat and A. Bell, *Angew. Chem., Int. Ed.*, 2007, **46**, 4477.

45. O. Linnenberg, P. Kozłowski, C. Besson, J. van Leusen, U. Englert and K. Y. Monakhov, *Cryst. Growth Des.*, 2017, **17**, 2342.

46. M. A. Augustyniak-Jablokow, S. A. Borshch, C. Daniel, H. Hartl and Y. V. Yablokov, *New J. Chem.*, 2005, **29**, 1064.

47. P. Lapham, L. Vila-Nadal, L. Cronin and V. P. Georgiev, *J. Phys. Chem. C* 2021, **125**, 3599.

48. R. Tsunashima, I. Nakamura, R. Oue, S. Koga, H. Oki, S. I. Noro, T. Nakamura and T. Akutagawa, *Dalton. Trans.*, 2017, **46**, 12619.

49. J. D. Rinehart and J. R. Long, *Chem. Sci.*, 2011, **2**, 2078.

50. a) D. Komijani, A. Ghirri, C. Bonizzoni, S. Klyatskaya, E. Moreno-Pineda, M. Ruben, A. Soncini, M. Affronte and S. Hill, *Phys. Rev. Mater.*, 2018, **2**, 024405; b) T. Ishida,T. Nakamura, T. Kihara and H. Nojiri, *Polyhedron*, 2017, **136**, 149; c) M. Urdampilleta, S. Klayatskaya, M. Ruben and W. Wernsdorfer, *ACS Nano*, 2015, **9**, 4458; d) H. Huang, W. Van den Heuvel and A. Soncini, *Quantum Mater. Res.*, 2020, **1**, e200003, and references therein.

51. S. Rast, A. Borel, L. Helm, E. Belorizky, P. H. Fries and A. E. Merbach, *J. Am. Chem. Soc.*, 2001, **123**, 2637.

52. X. Zhang, H. Xie, M. Ballesteros-Rivas, T. J. Woods and K. R. Dunbar, *Chem. Eur. J.*, 2017, **23**, 7448.

53. W. D. Oliver and P. B. Welander, *MRS Bulletin*, 2013, **38**, 816.

54. D. Van Der Spoel, E. Lindahl, B. Hess, G. Groenhof, A. E. Mark and H. J. Berendsen, *J. Comput. Chem.*, 2005, **26**, 1701.

55. B. Hess, C. Kutzner, D. van der Spoel and E. Lindahl, *J. Chem. Theory Comput.*, 2008, **4**, 435.

56. J. Wang, P. Cieplak and P. A. Kollman, *J. Comput. Chem.*, 2000, **21**, 1049.

57. A. Chaumont and G. Wipff, *J. Phys. Chem. C*, 2009, **113**, 18233.

58. P. Jiménez-Lozano, A. Solé-Daura, G. Wipff, J. M. Poblet, A. Chaumont and J. J. Carbó, *Inorg. Chem.*, 2017, **56**, 4148.

59. G. Toupalas, J. Karlsson, F. A. Black, A. Masip-Sánchez, X. López, Y. Ben M'Barek, S. Blanchard, A. Proust, S. Alves, P. Chabera, I. P. Clark, T. Pullerits, J. M. Poblet, E. A. Gibson and G. Izzet, *Angew. Chem., Int. Ed.*, 2021, **60**, 6518.

60. G. te Velde, F. M. Bickelhaupt, E. J. Baerends, C. Fonseca Guerra, S. J. A. van Gisbergen, J. G. Snijders and T. Ziegler, *J. Comput. Chem.*, 2001, **22**, 931.

61. ADF 2019.3, SCM, Theoretical Chemistry, Vrije Universiteit, Amsterdam, The Netherlands, *http://www.scm.com*.

62. M. Swart, A. W. Ehlers and K. Lammertsma, *Mol. Phys.*, 2004, **102**, 2467.

63. A. D. Becke, *J. Chem. Phys.*, 1993, **98**, 5648.

64. P. J. Stephens, F. J. Devlin, C. F. Chabalowski and M. J. Frisch, *J. Phys. Chem. A*, 1994, **98**, 11623.

65. E. v. Lenthe, E. J. Baerends and J. G. Snijders, *J. Chem. Phys.*, 1993, **99**, 4597.

66. E. van Lenthe, E. J. Baerends and J. G. Snijders, *J. Chem. Phys.*, 1994, **101**, 9783.

67. E. van Lenthe, A. Ehlers and E.-J. Baerends, *J. Chem. Phys.*, 1999, **110**, 8943.

68. C. C. Pye and T. Ziegler, *Theor. Chem. Acc.*, 1999, **101**, 396.

69. G. V. Buxton, In *Radiation Chemistry – Principles and Applications*, eds. Farhataziz and M. A. J. Rodgers, VCH Publ. Inc., Weinheim, Germany, 1987, pp. 321–350.

70. P. Wardman, *J. Phys. Chem. Ref. Data*, 1989, **18**, 1637.

71. K. Ishii and N. Kobayashi, In *The Porphyrin Handbook*, eds. K. M. Kadish, K. M. Smith and R. Guilard, Academic Press, London, 2000, vol. 16, pp. 1–42.

72. A. Kahnt, In *Applications of Porphyrinoids as Functional Materials* eds. H. Lang and T. Rüffer, The Royal Society of Chemistry, 2021, p. 220–251.

73. D. M. Guldi, I. Zilbermann, A. Gouloumis, P. Vázquez and T. Torres, *J. Phys. Chem. B*, 2004, **108**, 18485.

74. S. FitzGerald, C. Farren, C. F. Stanley, A. Beeby and M. R. Bryce, *Photochem. Photobiol. Sci.*, 2002, **1**, 581.

75. C. Farren, S. FitzGerald, A. Beeby and M. R. Bryce, *Chem. Commun.*, 2002, 572.

76. H. Imahori, K. Hagiwara, M. Aoki, T. Akiyama, S. Taniguchi, T. Okada, M. Shirakawa and Y. Sakata, *J. Am. Chem. Soc.*, 1996, **118**, 11771.

77. M. Wolf, C. Villegas, O. Trukhina, J. L. Delgado, T. Torres, N. Martín, T. Clark and D. M. Guldi, *J. Am. Chem. Soc.*, 2017, **139**, 17474.

78. V. Nikolaou, F. Plass, A. Planchat, A. Charisiadis, G. Charalambidis, P. A. Angaridis, A. Kahnt, F. Odobel and A. G. Coutsolelos, *Phys. Chem. Chem. Phys.*, 2018, **20**, 24477.

79. V. E. Pyatosin and M. P. Tsvirko, *J. Appl. Spectrosc.*, 1980, **33**, 869.

80. M. E. El-Khouly, O. Ito, P. M. Smith and F. D'Souza, *J. Photochem. Photobiol. C: Photochem. Rev.*, 2004, **5**, 79.

81. T. Nyokong, Z. Gasyna and M. J. Stillman, *Inorg. Chem.*, 1987, **26**, 548.

82. E. Ough, Z. Gasyna and M. J. Stillman, *Inorg. Chem.*, 1991, **30**, 2301.

83. P. C. Minor, M. Gouterman and A. B. P. Lever, *Inorg. Chem.*, 1985, **24**, 1894.

84. W. Seitz, A. Kahnt, D. M. Guldi and T. Torres, *J. Porphyr. Phthalocyanines*, 2009, **13**, 1034.

85. E. Moreno-Pineda and W. Wernsdorfer, *Nat. Rev. Phys.*, 2021, **3**, 645.

86. M. Atzori and R. Sessoli, *J. Am. Chem. Soc.*, 2019, **141**, 11339.

87. M. R. Wasielewski, M. D. E. Forbes, N. L. Frank, K. Kowalski, G. D. Scholes, J. Yuen-Zhou, M. A. Baldo, D. E. Freedman, R. H. Goldsmith, T. Goodson, M. L. Kirk, J. K. McCusker, J. P. Ogilvie, D. A. Shultz, S. Stoll and K. B. Whaley, *Nat. Rev. Chem.*, 2020, **4**, 490.

88. E. Coronado, *Nat. Rev. Mat.*, 2020, **5**, 87.

89. R. Ishikawa, S. Michiwaki, T. Noda, K. Katoh, M. Yamashita and S. Kawata, *Magnetochemistry*, 2019, **5**, 30.

90. H. Wada, S. Ooka, D. Iwasawa, M. Hasegawa and T. Kajiwara, *Magnetochemistry*, 2016, **2**, 43.

91. C. V. Topping and S. J. Blundell, *J. Phys. Condens. Matter*, 2019, **31**, 013001.

92. Y. S. Ding, K. X. Yu, D. Reta, F. Ortu, R. E. P. Winpenny, Y. Z. Zheng and N. F. Chilton, *Nat. Commun.*, 2018, **9**, 3134.

93. E. Bartolome, A. Arauzo, J. Luzon, J. Bartolome and F. Bartolome, In *Handbook of Magnetic Materials*, ed. E. Brück, North Holland, Amsterdam, 2017, vol. 26, pp. 1–289.

94. D. Aravena, *J. Phys. Chem. Lett.*, 2018, **9**, 5327.

95. A. Ardavan, O. Rival, J. J. Morton, S. J. Blundell, A. M. Tyryshkin, G. A. Timco and R. E. Winpenny, *Phys. Rev. Lett.*, 2007, **98**, 057201.

96. M. A. Sorensen, U. B. Hansen, M. Perfetti, K. S. Pedersen, E. Bartolome, G. G. Simeoni, H. Mutka, S. Rols, M. Jeong, I. Zivkovic, M. Retuerto, A. Arauzo, J. Bartolome, S. Piligkos, H. Weihe, L. H. Doerrer, J. van Slageren, H. M. Ronnow, K. Lefmann and J. Bendix, *Nat. Commun.*, 2018, **9**, 1292.

97. A. Gaita-Ariño, F. Luis, S. Hill and E. Coronado, Nat. Chem., 2019, **11**, 301.

98. A. Palii, S. Aldoshin, B. Tsukerblat, J. J. Borràs-Almenar, J. M. Clemente-Juan, S. Cardona-Serra and E. Coronado, *Inorg. Chem.*, 2017, **56**, 9547.
99. T. Miura, D. Fujiwara, K. Akiyama, T. Horikoshi, S. Suzuki, M. Kozaki, K. Okada and T. Ikoma, *J. Phys. Chem. Lett.*, 2017, **8**, 661.
100. S. Cardona-Serra, J. M. Clemente-Juan, E. Coronado, A. Gaita-Ariño, N. Suaud, O. Svoboda, R. Bastardis, N. Guihéry and J. J. Palacios, *Chem. Eur. J.*, 2015, **21**, 763.